Theory of Stimulated Brillouin Scattering in Fibers for Highly Multimode Excitations

Kabish Wisal,[1] Stephen C. Warren-Smith,[2] Chun-Wei Chen,[3] Hui Cao,[3] and A. Douglas Stone[3,*]
[1]*Department of Physics, Yale University, New Haven, Connecticut 06520, USA*
[2]*Future Industries Institute, University of South Australia, Mawson Lakes, South Australia 5095, Australia*
[3]*Department of Applied Physics, Yale University, New Haven, Connecticut 06520, USA*

(Received 18 April 2023; accepted 21 August 2024; published 26 September 2024)

Stimulated Brillouin scattering (SBS) is often an unwanted loss mechanism in both active and passive fibers. Highly multimode excitation of fibers has been proposed as a novel route toward efficient SBS suppression. Here, we develop a detailed, quantitative theory which confirms this proposal and elucidates the physical mechanisms involved. Starting from the vector optical and scalar acoustic equations, we derive appropriate nonlinear coupled mode equations for the signal and Stokes modal amplitudes and an analytical formula for the SBS (Stokes) gain with applicable approximations, such as the neglect of shear effects. This allows us to calculate the exponential growth rate of the Stokes power as a function of the distribution of power in a highly multimode signal. The peak value of the gain spectrum across the excited modes determines the SBS threshold—the maximum SBS-limited power that can be sent through the fiber. The theory shows that the peak SBS gain is greatly reduced by highly multimode excitation due to gain broadening and relatively weaker intermodal SBS gain. The inclusion of exact vector optical modes in the calculation is crucial in order to capture the incomplete intermodal coupling due to mismatch of polarization patterns of higher-order modes. We demonstrate that equal excitation of the 160 modes of a commercially available, highly multimode circular step index fiber raises the SBS threshold by a factor of 6.5 and find comparable suppression of SBS in similar fibers with a D-shaped cross section.

DOI: 10.1103/PhysRevX.14.031053 Subject Areas: Optics, Photonics

I. INTRODUCTION

Stimulated Brillouin scattering (SBS) is the nonlinear scattering of light by acoustic phonons generated by optical forces [1–5]. It was first theoretically predicted by Brillouin in 1922 [6] and experimentally demonstrated in liquids in 1964 [7] and in optical fibers in 1972 [8]. SBS has been utilized for diverse applications such as slow light [9], nonreciprocal light storage [10], strain and temperature sensing [11], phase conjugation and beam cleaning [12–14], Brillouin microscopy [15], Brillouin lasers [16], and integrated photonics [17–20]. On the other hand, SBS is often a highly undesirable effect in both active and passive systems. Of particular interest is its role in limiting the power capacity of narrow-linewidth high-power fiber lasers and high-power delivery fibers [3,21–24]. As input power is increased, SBS can cause almost complete reflection above a certain threshold power, rendering both active and passive fibers inoperable above that power level [2,3,8,25]. Significant research efforts have, therefore, been devoted to suppressing SBS efficiently. Because of concerns about maintaining high-output beam quality, almost all of the experimental and theoretical work has focused on exciting a single fundamental mode (FM) of the fiber [whether or not the fiber itself is nominally single-mode or multimode fiber (MMF)]. Recently, highly multimode excitation of fibers has been proposed as a novel route toward efficient suppression of SBS in both active and passive fibers [26–28]. In the current work, we explore theoretically the effect on SBS of highly multimode excitation of MMFs. While a number of previous works have introduced elements of our current theory [29–31], none have developed a quantitative formalism for computing SBS under highly multimode excitation, nor has any explored and identified the physical effects that arise when controlled, highly multimode signals are imposed.

As noted, most of the previous efforts to suppress SBS were in single-mode fibers and employed one of the following approaches: broadening the Brillouin spectrum by dynamic seed modulation [32–34] or applying temperature and strain gradients along the fiber [35,36], tailoring the fiber acoustic properties to reduce acousto-optic overlap [30,37–40], and altering the geometry (shape and composition) of the fiber cross section [41,42]. Although all of these efforts have had some success, they suffer from a number of drawbacks: For seed modulation, a large linewidth

*Contact author: douglas.stone@yale.edu

broadening [32–34] makes the resultant beams unsuitable for coherent beam combining and other narrow-band applications [43–45]; for acoustic mode tailoring, the need for precise fiber design and fabrication to control both the acoustic-index and optical-index profiles [30,37–40]; and for increased core size, the challenge of maintaining single-mode guidance with increasingly smaller numerical aperture and the emergence of other undesirable effects such as transverse mode instability [46].

The current investigation of a highly multimode approach was motivated by recent developments in the field of wavefront shaping, which have shown that (i) it is possible to control nonlinear effects by manipulating the input excitation in multimode fibers [47–51] and (ii) it is possible, even for multimode excitation, to obtain a high-quality output beam by wavefront shaping, since for a narrow input linewidth, the light in various fiber modes remains mutually coherent throughout the fiber [52–55]. Thus, multimode excitation combined with appropriate wavefront shaping can, in principle, provide a novel method of SBS suppression while maintaining good beam quality. Any desired output beam profile can be achieved even at high output powers by placing a spatial light modulator (SLM) at the fiber input, which would interact with relatively low seed power. The manipulation of output beam by input wavefront shaping in both passive fibers and fiber amplifiers have been demonstrated experimentally [28,54].

Previous studies, both experimental and theoretical, of SBS in few-mode fibers appear to support the viability of increasing the SBS threshold by using multimode excitation [56–60]. Moreover, several such studies indicate that intermodal SBS gain is weaker than intramodal gain [29,61–63]. This suggested that division of power in many modes may reduce the effective SBS gain within a given fiber; the efficacy of this approach is a key result of the theory and computational examples in the current work. Finally, assuming that the fiber is in the phase-matched limit, previous work [29,63] and our findings below show that the SBS threshold depends on only the input power in various modes, leaving the input phases of various modes as free parameters. Using wavefront shaping, these phases can, in principle, be carefully selected to control and focus the output beam profile via modal interference [28,54,64]. In order to understand the potential of power division and wavefront shaping for suppressing SBS in MMFs, we have developed a quantitative and computationally tractable theory of the effective SBS gain spectrum under highly multimode excitation. This theory is general enough to be applicable to other questions in the theory of multimode SBS, beyond maximizing the threshold such as in studying multimode Brillouin fiber sensors for temperature and strain sensing.

Most previous SBS theories assume single transverse mode operation for both the signal (which acts as the pump for Brillouin scattering) and Stokes field [2,3,31,65,66]. There have been efforts to model SBS in MMFs in the study of phase conjugation and beam cleaning using MMFs [12–14]. However, these approaches focus only on identifying the selection rules for nonzero mode couplings and do not model the individual couplings accurately. In particular, the guided nature of acoustic modes is generally ignored, resulting in inaccurate SBS thresholds. There is also extensive literature on SBS theory in nanowaveguides [5,17,30,67–70], although only a few studies focus on intermodal gain and none of them study multimode excitation. The most general previous theory of SBS in MMFs was done by Ke, Wang, and Tang [29]. They showed that, within the phase-matched regime, the power in each Stokes mode grows exponentially at a rate proportional to the signal power in various modes multiplied by the multimode Brillouin gain spectra, determined by the overlap of the optical and acoustic modes involved. The analysis by Ke, Wang, and Tang is, however, limited in important ways: First, it treats both acoustic and optical fields as scalar quantities; the latter is a problematic assumption, as we show below. Second, they did not undertake any explicit calculations of Brillouin gain spectra for a highly multimode excitation of a MMF. Hence, they did not study the major physics questions addressed in the current work, nor did they provide an accurate enough computational framework for doing so.

In this paper, we formulate a theory of SBS in MMFs starting from the full-field wave equations for electric and acoustic fields [69]. Finite-difference-based simulations of these equations have been used to model the SBS in the nanowaveguides [69]. In multimode fibers which are a few meters long, brute-force simulations of these equations are not feasible. We derive a semianalytical solution to these equations for arbitrary multimode excitations in fibers. The optical field equations are vector Helmholtz equations [71], sourced by a nonlinear polarization due to the photoelastic effect [72]. The acoustic field equations [73,74] are those of general continuum elasticity with the stiffness and viscosity tensors describing the restoring force and damping, respectively, and the driving source arising from optical forces generated due to electrostriction [75]. We demonstrate that, for accurate calculations of the SBS coupling in MMFs, it is important to take into account the vector nature of the optical fields and, in general, the acoustic modes. We find that for standard silica fibers (the focus of the current work), which are elastically isotropic, taking into account the vector nature of acoustic modes and the tensor shear forces is not crucial. However, as noted, the vector nature of optical modes plays a much more important role, and neglecting this can lead to errors (approximately 50%–100%) and qualitatively incorrect results for SBS threshold for multimode excitations. The scalar treatment of optical modes does not account for polarization mismatch and, therefore, overestimates the intermodal SBS coupling. As a result, it underestimates the decrease in effective SBS gain upon multimode excitation, predicting qualitatively incorrect results for SBS suppression in multimode fibers. Our formalism is general enough to permit the calculation of the SBS threshold for an arbitrary input excitation in MMFs, with any fiber cross section, refractive index profile, and fiber length. In particular, our theory is well suited to study the optimization of the SBS threshold with respect to degrees of freedom in MMFs. For example, we use our theory to calculate the SBS gain for all the approximately 10^4 mode pairs for an example corresponding to a commercially available highly multimode circular step-index fiber and find that, when all the modes are equally excited, a roughly 6.5×-higher SBS threshold can be obtained, compared to exciting only the fundamental mode. The physical origins of this stability enhancement is discussed and elucidated below.

The paper is organized as follows. In Sec. II, we start by deriving the coupled mode equations for Stokes and signal amplitudes, assuming only the translational invariance in z, the slowly varying envelope approximation, and highly damped phonons [2]. All of these approximations are valid for most multimode fibers. We do not assume phase matching *a priori*. Then we apply the undepleted-signal approximation [1], valid below SBS threshold, to obtain linear growth equations for each Stokes amplitude. This allows us to formulate a linearized theory of the SBS modal couplings which accurately captures the vector nature of all the fields involved.

In Sec. III, we systematically simplify the SBS coupling under a series of applicable approximations. We show that the length of the fiber compared to a phase-mismatch length scale determines whether phase-mismatched terms need to be kept or can be discarded. In the phase-matched limit, the equations for various Stokes modes decouple, leading to independent exponential growth in the backward direction. The rate of growth for power in each Stokes mode depends on the modal content of the signal and is given by a sum of signal power in each mode weighted by the corresponding Brillouin gain spectra (BGS), which now generalizes to a matrix of pairwise modal spectra. The BGS for a Stokes-signal pair is given by a sum of Lorentzians, for each acoustic mode, with peak values proportional to the overlap integrals of the Stokes, signal, and acoustic modes involved. We derive a reasonably accurate simplified form of the overlap integrals for elastically isotropic fibers with small shear acoustic velocities, where the dot product of the two vector optical modes appears in the integrand. This form is critical for accurately evaluating the intermodal gain, especially for large numerical aperture fibers, when the scalar, linearly polarized (LP) modes are not good approximations of exact vector fiber modes. Both intramodal and intermodal terms contribute to the growth rate of a given mode m in a manner determined by the signal power distribution. Hence, we introduce the important concept of an effective gain for each mode, $\tilde{g}_m(\Omega)$, which captures the effect of a particular signal power distribution on the gain experienced by a Stokes mode m. This allows us to define a generalized, signal-dependent formula for the SBS threshold for MMFs within the phase-matched theory.

In Sec. IV, we explicitly calculate the BGS for highly multimode step-index fibers with circular and D-shaped cross sections. We show that the SBS threshold is increased significantly if the input power is optimally distributed in multiple fiber modes, initially using a two-mode example. We show that this increase arises from two effects. First, the intermodal gain is typically weaker than the intramodal gain, due to the mismatch in different optical modal spatial and polarization profiles. This significantly decreases the effective SBS gain when multiple modes are excited. Second, the peaks of the BGS for different mode pairs are shifted relative to each other, since they are mediated by different acoustic modes; thus, power division among many modes tends to broaden the gain spectrum, leading to further SBS suppression [57]. Here, we present the example of exciting equally all 160 modes of a circular step-index fiber, leading to a 6.5×-higher SBS threshold, compared to exciting just the fundamental mode. Because of the distinct polarization properties of D-shaped fiber, we find that the increase of the SBS threshold in this case is dependent on the input polarization and is highest for input polarized at 45° with respect to the axis of symmetry, an effect which is explained by our theory.

Finally, in Sec. V, we provide a discussion of experimental validation, applicability, and future directions for our work.

II. MULTIMODE SBS MODEL

A. Coupled optical and acoustic equations

SBS is a result of optical scattering by acoustic phonons generated by electrostriction [1–3]. A schematic of the SBS in a fiber is shown in Fig. 1. The forward-going signal wave at frequency ω_1 interferes with a backward-going and Stokes-shifted wave at frequency $\omega_2 = \omega_1 - \Omega$, generating a moving intensity grating. This intensity pattern results in optical forces through electrostriction, which generate acoustic phonons with frequency Ω. These phonons, in turn, reflect light in the backward direction, leading to exponential growth in the Stokes power. To model SBS, we solve the optical and acoustic wave equations coupled through nonlinear source terms due to electrostriction and the photoelastic effect. The total electric field $\vec{E}$ satisfies the vector Helmholtz equation [68,69]:

$$\left[\nabla^2 - \frac{n^2}{c^2}\frac{\partial^2}{\partial t^2}\right]\vec{E} = \mu_0 \frac{\partial^2}{\partial t^2}(\chi_{\mathrm{N}}\vec{E}). \tag{1}$$

Here, n is the linear refractive index of the fiber, μ_0 is the free space permeability, c is the speed of light in vacuum, and χ_{N} is the nonlinear photoelastic susceptibility [72] and, in a sufficient approximation, is given by

$$\chi_{\mathrm{N}} = \gamma_{\mathrm{e}} \nabla \cdot \vec{u}, \tag{2}$$

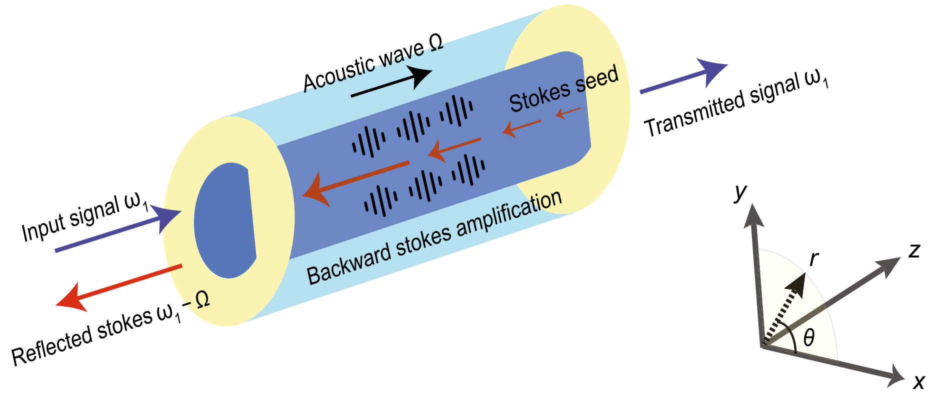

FIG. 1. Schematic of SBS in a multimode fiber with arbitrary core shape (here, D-shaped). Stokes-shifted backward-traveling light (seeded by spontaneous Brillouin scattering) experiences amplification due to the scattering of the forward-going signal by the acoustic phonons, which are generated by electrostriction. This process can take away significant power from the signal and limits the transmitted power.

where γ_e is the electrostriction constant and the isotropic part of the acoustic strain is given by the divergence of the acoustic displacement field $\vec{u}$. Here, we assume an isotropic fiber medium, where we find that isotropic (pressure) effects are dominant, and the shear effects have negligible impact on the nonlinear polarization for typical fibers, such as the silica multimode fibers considered below.

However, the formalism derived here in the main text can be straightforwardly generalized to the full tensor theory of elasticity, as shown in Appendix A, for both fibers or waveguides with significant shear effects. The electrostriction constant is replaced by the full photoelastic tensor contracted with the acoustic strain tensor, and a generalized acoustic equation is used which involves the elasticity and viscosity tensors. For isotropic fiber, these equations simplify but still include shear effects, which need to be evaluated. In Appendix A, we do this for standard silica fibers and show examples; we conclude that for such fibers the effects are small enough to neglect in the calculations reported in the main text.

When shear effects are negligible, the acoustic field can be described by scalar density fluctuations given by $\delta\rho = \rho_0 \nabla \cdot \vec{u}$, which satisfy a scalar acoustic equation:

$$\left[\left(V_L^2 + \tilde{\Gamma}\frac{\partial}{\partial t}\right)\nabla^2 - \frac{\partial^2}{\partial t^2}\right]\delta\rho = -\nabla \cdot \vec{F}. \tag{3}$$

Here, V_L is the longitudinal acoustic velocity, ρ_0 is the mean fiber density, and $\tilde{\Gamma}$ is the acoustic loss rate. The source term in the acoustic equation is proportional to the divergence of the optical force $\vec{F}$ and is given by [69]

$$\nabla \cdot \vec{F} = -\frac{1}{2}\gamma_e \nabla^2 (\vec{E} \cdot \vec{E}). \tag{4}$$

The optical force is proportional to the electrostriction constant γ_e and the gradient of the optical intensity given by the dot product of electric field $\vec{E}$ with itself. Note that the acoustic source term is quadratic in the optical field and the optical source term is also "quadratic" as the product of the optical field with the displacement field. We include only the electrostriction term in the optical force and χ_N and neglect the force generated due to the deformation of the fiber boundary [17,68,69]. This is justified if the core size of the fiber is much larger than the wavelength of light, which is typically the case for multimode fibers. Note that, unlike prior work on SBS in fibers, we retain the vector nature of the electric field in Eqs. (1) and (4), instead of assuming a uniform polarization with scalar profile. We find that using the full vector optical modes is critical for accurate calculation of Brillouin scattering between different modes with different (and spatially varying) polarization profiles. In Appendix B, we show that qualitatively incorrect results for the SBS threshold are obtained in the scalar approximation.

B. Modal decomposition and acoustic mode elimination

To study the Stokes growth, we split the total electric field $\vec{E} = \vec{E}_1 + \vec{E}_2$ into a forward-going signal wave $\vec{E}_1$ and a backward-going Stokes wave $\vec{E}_2$. Assuming the refractive index is translationally invariant along the fiber axis, we can decompose both $\vec{E}_1$ and $\vec{E}_2$ in terms of relevant vector fiber modes [76–78] with slowly varying amplitudes [2]:

$$E_1 = \sum_m A_m(z,t)\vec{f}_m^{(1)}(r,\theta)e^{i(\omega_1 t - \beta_m z)} + \text{c.c.},$$
$$E_2 = \sum_m B_m(z,t)\vec{f}_m^{(2)}(r,\theta)e^{i(\omega_2 t + \gamma_m z)} + \text{c.c.} \tag{5}$$

Here, β_m (γ_m) and $\vec{f}_m^{(1)}(r,\theta)$ [$\vec{f}_m^{(2)}(r,\theta)$] denote the propagation constant in the z direction and the transverse mode profile for the mth signal (Stokes) mode, respectively. ω_1 is the signal frequency, ω_2 is the Stokes frequency, and the

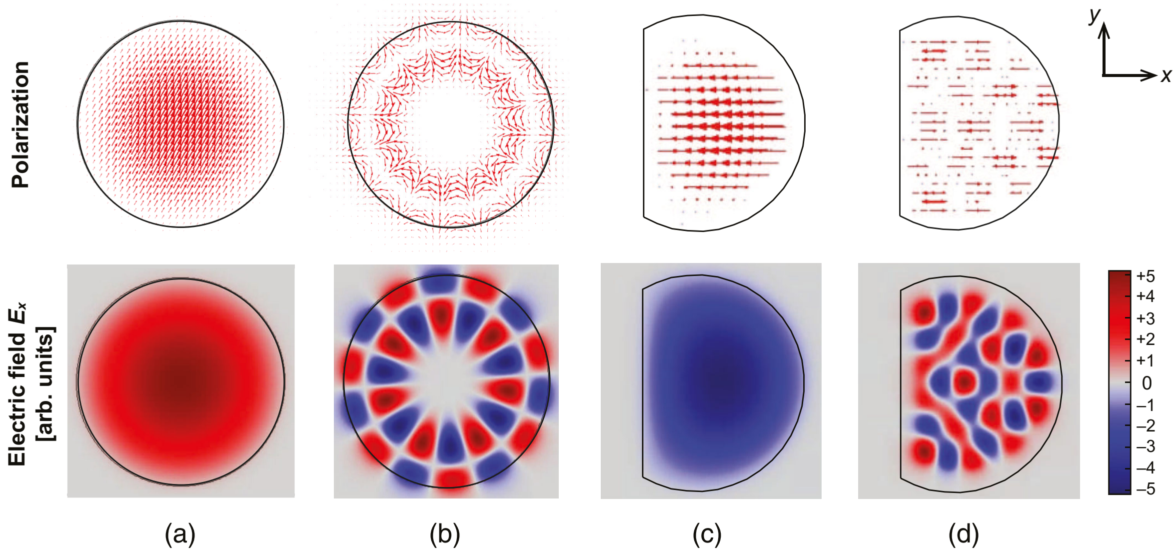

FIG. 2. Polarization (upper) and x component of the electric field, E_x (lower) profiles for fundamental (a),(c) and higher-order (b),(d) optical modes of step-index multimode fibers with circular (a),(b) and D-shaped (c),(d) core cross sections. Note the more ergodic behavior of the D fiber modes compared to the circular case. Modes of the circular cross-section fiber have spatially varying polarization depending on the mode. Modes of the fiber with a D-shaped cross section have polarization either along the axis of symmetry (x axis) or orthogonal to it (y axis).

difference of the two frequencies, $\Omega = \omega_1 - \omega_2$, represents the Stokes shift. The transverse modes satisfy the vector fiber modal equations given by [77,78]

$$\left[\nabla_{\mathrm{T}}^2 + \left(\frac{n^2\omega_1^2}{c^2} - {\beta_m}^2\right)\right]\vec{f}_m^{(1)}(r,\theta) = 0,$$
$$\left[\nabla_{\mathrm{T}}^2 + \left(\frac{n^2\omega_2^2}{c^2} - {\gamma_m}^2\right)\right]\vec{f}_m^{(2)}(r,\theta) = 0. \qquad (6)$$

The solution for the mode profiles and the corresponding propagation constants can be obtained analytically in the case of a circular step-index geometry [77,78] or numerically for an arbitrary fiber cross section and refractive index profile. In Fig. 2, we plot the polarization and the x component of the electric field for the fundamental and a higher-order mode in step-index fibers with circular and D-shaped cross sections. The fields are determined using the finite element method in the wave optics module of COMSOL MULTIPHYSICS (version 5.5) [79]. In general, both the electric field amplitude and the polarization vary spatially for the different modes. For the circular fiber, the fundamental mode [Fig. 2(a)] is approximately uniformly polarized, while higher-order modes [Fig. 2(b)] have spatially varying polarization with azimuthal and radial components. For the D-shaped fibers, modes are approximately uniformly polarized either along the axis of symmetry (x polarized) or orthogonal to it (y polarized) for both the fundamental mode [Fig. 2(c)] and the higher-order modes [Fig. 2(d)]. The choice to study D-shaped core fibers, in particular, is motivated by chaotic ray dynamics in D-shaped cavities [80], leading to more ergodic field profiles, especially for significantly higher-order modes.

We normalize both the signal and Stokes modes such that the power in the mth signal and Stokes modes is proportional to $|A_m|^2$ and $|B_m|^2$, respectively. The interference between the signal and Stokes fields gives rise to an acoustic source term for each signal-Stokes pair $\{i,j\}$ which oscillates at frequency Ω and has propagation constant $q_{ij} = \beta_i + \gamma_j$ in the z direction. Therefore, we expand the density fluctuation into a series of acoustic modes $\{k\}$ for each source term $\{i,j\}$:

$$\delta\rho = \sum_{i,j}\sum_{k} c_k^{ij}(z,t) g_k^{ij}(r,\theta) e^{i(\Omega t - q_{ij}z)} + \text{c.c.} \qquad (7)$$

Here, $c_k^{ij}(z,t)$ is the slowly varying amplitude for the kth acoustic mode corresponding to optical pair $\{i,j\}$. The associated transverse mode profile is given by $g_k^{ij}(r,\theta)$, which satisfies the following modal equation [68]:

$$\left[\nabla_{\mathrm{T}}^2 + \left(\frac{\Omega_{ijk}^2}{v_L^2} - q_{ij}^2\right)\right] g_k^{ij}(r,\theta) = 0. \qquad (8)$$

Here, ∇_{T} is the transverse gradient operator. We choose to not include the acoustic loss given by $\tilde{\Gamma}$ explicitly in the modal equation; it is accounted for through the coefficients c_{ij}^k. This choice has an advantage that it allows the operator of the modal equation to be Hermitian, which leads to useful properties such as orthogonality and completeness of the modal basis [71].

To obtain the solution for the acoustic field, $\delta\rho$, we evaluate source terms in Eq. (3) using Eqs. (4) and (5).

The left-hand side of Eq. (3) can be simplified by substituting the ansatz for $\delta\rho$ from Eq. (7). We multiply with acoustic mode profile g_k^{ij*} and utilize orthogonality of acoustic modes to isolate the equation for a single acoustic amplitude. Upon applying the slowly varying approximation, where we ignore the second-order z derivatives of c_k^{ij} and using the modal equations [Eq. (8)], we get the following equation:

$$\left[2iq_{ij}\frac{\partial}{\partial z} + 2i\Omega\frac{\partial}{\partial t} + (\Omega_{ijk}^2 - \Omega^2 + i\Omega\Gamma)\right]c_k^{ij} = -\frac{O_1}{2}A_i B_j^*, \tag{9}$$

where O_1 denotes the overlap integral of the source term with the relevant acoustic mode and is given by

$$O_1 = -q_{ij}^2\gamma_e\langle(\vec{f}_i^{(1)} \cdot \vec{f}_j^{(2)*})g_k^{ij*}\rangle. \tag{10}$$

The angular brackets $\langle.\rangle$ denote integration over the entire fiber cross section. To study the steady-state behavior, we set the time derivative in Eq. (9) to zero. Also, the typical phonon propagation length in fibers is much smaller than the fiber length [1,2]. Thus, SBS is effectively mediated by localized phonons, which allows us to drop the z derivative term in Eq. (9) as well. In that case, the acoustic modal coefficients are simplified to

$$c_k^{ij} = -\frac{1}{2}\frac{O_1}{\Omega_{ijk}^2 - \Omega^2 + i\Omega\Gamma}A_i B_j^*. \tag{11}$$

Here, we define a renormalized acoustic loss $\Gamma = q^2\tilde{\Gamma}$, where $q = 4\pi n/\lambda$. We drop weak modal dependence of Γ by assuming $q_{ij} \approx q$. This completes a formal solution for the acoustic field in terms of amplitudes of the signal and Stokes fields and the relevant overlap integrals, assuming acoustic modes have been solved either numerically or analytically [using Eq. (8)]. For special cases, such as elastically isotropic, circular, step-index fibers, it is possible to obtain acoustic modes semianalytically [31,81]. However, in general, for arbitrary fiber geometries and refractive index profiles, they can be obtained using a numerical solver such as COMSOL [79].

C. Coupled modal equations

We can now use the acoustic field to determine the source terms in the optical equation [Eq. (1)] and obtain coupled modal equations for the optical fields. The left-hand side of Eq. (1) can be simplified by substituting the modal decomposition of the electric field as given in Eq. (5) and using the optical modal equations [Eq. (6)]. The equation for a particular mode m can be isolated by taking a dot product with $\vec{f}_m^*$ and integrating over the fiber cross section. This leads to the following coupled amplitude equations:

$$-\frac{dB_m(\Omega)}{dz} = \sum_{i,j,l} Y_{mlij}(\Omega)A_l A_i^* B_j e^{i(\beta_i+\gamma_j-\beta_l-\gamma_m)z}, \tag{12}$$

$$\frac{dA_l(\Omega)}{dz} = \sum_{i,j,m} X_{lmji}(\Omega)B_m B_j^* A_i e^{-i(\beta_i+\gamma_j-\beta_l-\gamma_m)z}. \tag{13}$$

These are scalar, one-dimensional, ordinary differential equations in z, which accurately describe the acousto-optic interaction in a guided, translationally invariant in z, material system. The growth in each Stokes amplitude B_m is proportional to the sum of the products of two signal amplitudes, A_l and A_i^*, and a Stokes amplitude, B_j. The strength of each contribution depends on both a phase-mismatch factor and a coupling coefficient, $Y_{mlij}(\Omega)$, which has a resonant frequency dependence and quantifies how efficiently the optical and acoustic modes in the source terms overlap with each other. The transverse dependence and vector nature of the interaction are contained within the coupling coefficients Y_{mlij} and X_{lmji}, given by, respectively,

$$Y_{mlij} = \sum_k \frac{\mu_0\omega_2}{4n^2\rho_0\epsilon_0}\frac{O_1^* O_2}{-i(\Omega_{ijk}^2 - \Omega^2) + \Omega\Gamma},$$
$$X_{lmji} = \sum_k \frac{\mu_0\omega_1}{4n^2\rho_0\epsilon_0}\frac{O_1 O_2^*}{-i(\Omega_{ijk}^2 - \Omega^2) - \Omega\Gamma}. \tag{14}$$

The coupling coefficient for a particular four-wave-mixing term $\{m, l, i, j\}$ is a sum of Lorentzians for each acoustic mode, k, with a center frequency given by the eigenfrequency of the acoustic mode, Ω_{ijk}, and the linewidth given by the effective acoustic loss Γ. The peak value of the curves is proportional to the overlap integrals O_1 and O_2, where O_1 is given in Eq. (10). The second overlap integral O_2 is the projection of the optical source term onto the modal basis and has a similar form to O_1:

$$O_2 = \gamma_e\langle(\vec{f}_l^{(1)} \cdot \vec{f}_m^{(2)*})g_k^{ml*}\rangle. \tag{15}$$

The only assumptions we have used so far are translational invariance, neglecting the moving boundary terms [17], slowly varying approximation [1], and damped phonon approximation [1]. To the best of our knowledge, this is the first time these equations have been derived at this level of generality, for acousto-optic interactions in multimode, translationally invariant systems. These equations accurately capture the acousto-optic interaction at any length scale for arbitrary input excitations in multimode fibers, with any cross-section geometry. The equations can be integrated numerically much more efficiently than the original 3D nonlinear coupled optical and acoustic wave equations. This is because here the transverse degrees of freedom need to be accounted for only once (in the modal equations), due to the translational invariance in the longitudinal direction.

D. Undepleted signal

Despite the simplifications due to translational invariance imposed above, the general coupled mode equations for Stokes and signal amplitudes derived above are nonlinear equations and are difficult to solve analytically. However, for analyzing the question of the threshold for significant SBS loss, we can assume that the Stokes amplitudes are much smaller than the signal amplitudes. The SBS threshold is typically defined as when the power of the backward-going Stokes waves reaches a few percent of the signal power [2,3]. In this limit, the decay in signal power, *due to SBS*, is negligible; with this undepleted signal approximation, the signal modal amplitudes can be assumed to be constants, determined by the input. The equations for the Stokes amplitudes then become a set of *linear* ordinary differential equations and can be rewritten in the following matrix representation:

$$-\frac{dB(\Omega)}{dz} = M(z,\Omega)B(\Omega). \tag{16}$$

Here, $B(\Omega)$ is an $\mathrm{N} \times 1$ column vector with the mth entry equal to the Stokes amplitude, $B_m(\Omega)$. N is the total number of optical modes in the fiber. The coupling matrix $M(z,\Omega)$ is an $\mathrm{N} \times \mathrm{N}$ matrix whose entries are given by

$$M_{mj} = \sum_{il} Y_{mlij} A_l A_i^* e^{i(\beta_i+\gamma_j-\beta_l-\gamma_m)z}. \tag{17}$$

Equation (16) is a coupled linear system of first-order, homogeneous ordinary differential equations; its solution is given by

$$B(z) = \mathcal{P}\exp\left[\int_L^z M(z')dz'\right]B(L), \tag{18}$$

where the Stokes amplitude vector B at any point z is given by the path-ordered exponential [82] of the mode-coupling matrix M times the Stokes amplitude vector at the output end of the fiber, $B(L)$, which is typically seeded by the spontaneous Brillouin scattering. At this level of approximation, the Stokes amplitudes in various modes remain coupled, so that the growth of each B_m is affected by all the others. The signal amplitudes and the fiber properties act as parameters in the Stokes growth through the coupling matrix $M(z,\Omega)$. In principle, these equations can be used to evaluate the contribution of non-phase-matched and quasi-phase-matched terms in the growth equations at length scales where they are non-negligible.

III. PHASE-MATCHING LIMIT

A. Phase-matched Stokes power growth

The coupling matrix M_{mj} dictates the effect of Stokes amplitude B_j on the growth of Stokes amplitude B_m. Most of the elements of M have complex phases, which vary on the length scale given by the mismatch of longitudinal wave vectors (propagation constants) for the modes involved. Typically, these terms grow only over length scales in the range of 10^{-6}–10^{-3} m, whereas the total fiber length in realistic experiments with high average power is much greater than these length scales ($L \sim 1$–100 m). As a result, the terms with complex phases oscillate along the fiber axis and have significantly lower magnitude compared to the phase-matched terms, which grow exponentially. In this limit, the effect of phase-mismatched terms becomes negligible compared to phase-matched terms and, thus, can be neglected. We focus on this limit for the remainder of this work. The condition for phase matching of terms can be obtained directly from Eq. (17):

$$\beta_i + \gamma_j - \beta_l - \gamma_m = 0. \tag{19}$$

A straightforward solution to this condition is $i = l$, $j = m$. This solution corresponds to transfer of power from signal mode l to Stokes mode m. Note that there can be alternate solutions to the phase-matching equation. For instance, when there are exactly degenerate modes in the fiber, i.e., two different modes have the same propagation constant, there are more solutions to Eq. (19). We call them "nontrivially phase-matched terms." Since exact degeneracies are usually lifted in realistic step-index fibers due to fabrication imperfections, these alternate phase-matching solutions are typically absent. Note that in graded-index fibers there can be a significantly large number of degenerate modes, in which case this assumption is not applicable. When the exact degeneracies are present, all the solutions need to be included for maintaining consistency in the theory. For an ideal circular step-index fiber, the near degeneracy of the vector modes within the same group [77] gives rise to the nontrivially phase-matched terms over relevant length scales, which provides a connection between the vector and scalar SBS theories (see Appendix B for more details). For the rest of this work, we assume that in real materials any exact symmetries are broken and, thus, there are no exactly degenerate solutions for the propagation constants leading to the uniqueness of the $i = l$, $j = m$ solution. This leads to a dramatic simplification of the Stokes growth equations. The coupling matrix becomes diagonal ($m = j$), leading to independent growth for each of the Stokes amplitudes:

$$-\frac{dB_m(\Omega,z)}{dz} = \left[\sum_l Y_{mllm\times}(\Omega)|A_l|^2\right]B_m(\Omega,z). \tag{20}$$

The growth rate of Stokes amplitude m is proportional to the signal power in various modes, l, weighted by effective coupling Y_{mllm}. The Stokes amplitude growth equations can be converted to the growth equations for Stokes power by multiplying with the complex conjugate of the Stokes amplitude on both sides and adding the complex conjugate term, leading to

$$\frac{dP_m^{\mathrm{s}}(\Omega,z)}{dz} = -\left[\sum_l g_{\mathrm{B}}^{(m,l)}(\Omega)\tilde{P}_l\right]P_0 P_m^{\mathrm{s}}(\Omega,z) \equiv -\tilde{g}_m(\Omega)P_0P_m^{\mathrm{s}}(\Omega,z), \tag{21}$$

where $P_m^{\mathrm{s}}(\Omega,z)$ is the Stokes power in mode m, $\tilde{P}_l$ is the fraction of signal power in mode l ($\sum_l \tilde{P}_l = 1$), P_0 is the total signal power, Ω is the Stokes frequency shift, and $g_{\mathrm{B}}^{(m,l)}(\Omega)$ is the BGS for Stokes-signal mode pair (m,l). The Stokes power in each mode grows independently in the backward direction. Here, we define for each Stokes mode m an effective BGS $\tilde{g}_m(\Omega)$, which is equal to the weighted sum of pairwise BGS $g_{\mathrm{B}}^{(m,l)}(\Omega)$ with weights equal to the fractional signal power $\tilde{P}_l$ in various modes. Both the pairwise and effective BGS have units of [W^{-1} m^{-1}]. We see below that the effective BGS $\tilde{g}_m(\Omega)$ is physically meaningful; it is the engineered Brillouin spectrum for the mode m induced by our choice of input power distribution into signal modes and can be used to understand the increase in the SBS threshold due to multimode excitation.

The pairwise BGS $g_{\mathrm{B}}^{(m,l)}$ depends on the fiber properties and is equal to twice the real part of coupling coefficient Y_{mllm}; thus, it can be calculated using Eq. (14):

$$g_{\mathrm{B}}^{(m,l)}(\Omega) = G_0\sum_k |O_{mlk}|^2 \frac{\frac{\Gamma}{2}}{(\Omega_{mlk}-\Omega)^2 + (\frac{\Gamma}{2})^2}. \tag{22}$$

Here, G_0 is a constant including various material and optical constants and is given by $G_0 = (8\pi^3 c\mu_0\gamma_e^2/\lambda^3\rho_0\epsilon_0\Omega)$. The BGS for mode pairs (m,l) is a sum of Lorentzian curves for each acoustic mode k with a center frequency equal to the acoustic eigenfrequency Ω_{mlk}, and the linewidth is equal to effective acoustic loss Γ. Each acoustic mode contribution is weighted by $|O_{mlk}|^2$, the corresponding overlap integral of the optical and acoustic modes involved, given by

$$O_{mlk} = \langle(\vec{f}_l^{(1)}\cdot\vec{f}_m^{(2)*})g_k^{ml*}\rangle. \tag{23}$$

The presence of the dot product between the optical mode profiles is a key difference from standard scalar SBS theories [29] and is crucial for accurate calculation of the BGS under multimode excitation. For single-mode fibers, ($l = m$), the dot product simply reduces to scalar multiplication of modes, making a scalar SBS treatment acceptable. For multimode fibers, the polarization for different modes can be significantly different and spatially varying (see Fig. 2). We find that correctly evaluating this dot product is necessary to obtain accurate results for the intermodal gain ($l \neq m$). Specifically, the scalar treatment consistently overestimates the intermodal gain, an effect which was reported in Ref. [29], where they were able to compare the predicted scalar intermodal gain to experimentally measured values. For instance, the scalar theory predicted the intermodal coupling coefficient between modes $\mathrm{LP}_{0,1}$ and $\mathrm{LP}_{1,1}$ to be $0.51\ \mathrm{m}^{-1}\ \mathrm{W}^{-1}$, which was 50% higher than the experimentally measured value of $0.36\ \mathrm{m}^{-1}\ \mathrm{W}^{-1}$. In addition, we find that, for two-mode excitation of the fibers studied in Refs. [29,63], the vector theory predicts the highest SBS threshold occurs for a superposition of the two modes. This contrasts with the findings of the scalar theory, where single HOM excitation has the highest threshold [29,63]. We discuss these findings in detail in Appendix B and give the conditions when the scalar theory is accurate, as well as two examples of when it fails to reproduce results predicted by our vectorial treatment.

Finally, we can solve Eq. (21) to derive the exponential growth in Stokes power in various modes:

$$P_m^{\mathrm{s}}(\Omega,0) = P_m^{\mathrm{s}}(\Omega,L)e^{\tilde{g}_m(\Omega)P_{\mathrm{out}}L_{\mathrm{eff}}}. \tag{24}$$

The Stokes power in each mode grows exponentially in the backward direction with a growth rate equal to the effective BGS $\tilde{g}_m$ multiplied by the total output signal power P_{out}. We define an effective fiber length which takes into account the absorption in the fiber, $L_{\mathrm{eff}} = L(1-e^{-\alpha L}/\alpha L)$, where L is the fiber length and α is the absorption coefficient [2]. In the limit of small absorption, $\alpha L \ll 1$, we recover $L_{\mathrm{eff}} \approx L$, and when absorption is large $\alpha L \gg 1$, we get $L_{\mathrm{eff}} \approx 1/\alpha$.

B. Multimode SBS threshold

The SBS threshold is typically defined as the output signal power at which the backward-reflected Stokes power becomes a non-negligible fraction (typically, $> 1\%$) of the signal power [1–3,63]. We can use the Stokes growth equation derived in Sec. II A [Eq. (24)] to obtain the formula for the multimode SBS threshold. We assume SBS is seeded by spontaneous Brillouin scattering at the far end of the fiber, which leads to average photon density of one photon per mode in all the modes of the fiber. We set the threshold to be when the ratio of exponentially amplified Stokes power over the total signal power is equal to $\xi = 1\%$. The seed power from spontaneous Brillouin scattering is typically multiple orders of magnitude smaller than the signal power; thus, the amplification factor required to reach SBS threshold is very high. The mode with the highest Stokes growth rate, thus, exponentially dominates the Stokes power and can be used to approximate the total reflected power. Therefore, the threshold condition becomes

$$P^{\mathrm{s}} = P_{\mathrm{N}}e^{P_{\mathrm{th}}L_{\mathrm{eff}}g_{\mathrm{B}}} = \xi P_{\mathrm{th}}, \tag{25}$$

which can be rearranged as

$$P_{\mathrm{th}}L_{\mathrm{eff}}g_{\mathrm{B}} = \log\left(\frac{\xi P_{\mathrm{th}}}{P_{\mathrm{N}}}\right), \tag{26}$$

where P_{th} is the SBS threshold, L_{eff} is the effective length of the fiber taking into account the fiber absorption, and P_{N} is the Stokes noise power seeded by the spontaneous Brillouin scattering. We have introduced an overall Brillouin gain coefficient g_{B} which is equal to

$$g_{\mathrm{B}} \approx \max_{\Omega,m} \tilde{g}_m(\Omega) = \max_{\Omega,m} \sum_l g_{\mathrm{B}}^{(m,l)}(\Omega)\tilde{P}_l. \tag{27}$$

The SBS threshold is inversely proportional to the length of the fiber and the overall Brillouin gain coefficient g_{B}. It also weakly (logarithmically) depends on the output power level, seed power, and the fraction (ξ) at which the threshold is set. Additionally, we approximate the final Stokes power by the Stokes power in the mode with the highest growth rate, which is justified due to the exponential nature of the growth. In case there are multiple modes (say, M_s) with similar growth rates, the Stokes power will be M_s times higher than our estimation, which will lead to a $\log(M_s)$ correction to the effective SBS gain and threshold, which we find to be quite small. It can be verified that the multimode threshold formula in Eq. (26) reduces to the formula for single-mode fiber when only the fundamental mode is present. More generally, however, the SBS threshold depends on both the fiber properties [through $g_{\mathrm{B}}^{(m,l)}(\Omega)$] and the distribution of power in various signal modes, $\{\tilde{P}_l\}$. Our formalism allows an efficient calculation of the SBS threshold for different input multimode excitations for highly multimode fibers with any cross section. In addition, this formalism allows the investigation of SBS suppression by using highly multimode excitation to vary the power distribution in the signal modes at the input, a restricted form of wavefront shaping. In the next section, we show that by distributing power in multiple modes it is possible to substantially reduce the effective SBS gain, since $g_{\mathrm{B}}^{(m,l)}$ strongly depends on mode indices (l,m). This leads to a significant increase in SBS threshold with the number of excited modes when all the modes are equally excited.

IV. NUMERICAL RESULTS

In summary, we have shown that in a MMF the Stokes power in each mode grows exponentially with a growth rate equal to the total signal power multiplied with the effective BGS [Eq. (24)]. Therefore, the effective BGS and the SBS threshold [Eq. (26)] in a MMF depend on both the input signal power distribution $\{\tilde{P}_l\}$ and the pairwise BGS $g_{\mathrm{B}}^{(m,l)}(\Omega)$. For a given Stokes mode m and signal mode l, the BGS can be calculated by the formula given in Eq. (22). The BGS for each mode pair is a sum of Lorentzians corresponding to individual acoustic modes, weighted by the overlap of the optical and acoustic modes. For elastically isotropic fibers, we identify a simplified form of the overlap integral, which is reasonably accurate for calculating BGS, involving a dot product of the vector optical modes multiplied with a scalar acoustic eigenmode [Eq. (23)]. These equations [Eqs. (22), (24), (26), and (23)] are sufficient to determine the SBS threshold for a given multimode fiber for any input multimode excitation.

TABLE I. Detailed parameters for fiber A.

Parameter	Fiber A
Core shape	Circular
Core radius (μm)	10
Cladding radius (μm)	50
Core refractive index	1.4803
Cladding refractive index	1.4496
$\Delta\left(=\frac{n_{co}^2-n_{cl}^2}{n_{co}^2}\right)$	0.041
Signal wavelength (μm)	1.064
Number of optical modes	160
Core acoustic velocity V_L (m/s)	4946
Core acoustic velocity (shear) V_s (m/s)	3189
Cladding acoustic velocity V_L (m/s)	5944
Cladding acoustic velocity (shear) V_s (m/s)	3749
Number of acoustic modes	≥1000

The extent to which the input power division influences the SBS threshold is determined by the fiber properties through the pairwise BGS, $g_{\mathrm{B}}^{(m,l)}$. To study the properties of the pairwise BGS, we calculate the BGS for all the mode pairs for a highly multimode circular step-index fiber. We consider a commercially available fiber (fiber A) with germanium-doped silica core and pure silica cladding. The core radius of the fiber is 10 μm and with a numerical aperture of 0.30, supporting 160 optical modes. The detailed parameters are given in Table I.

To illustrate key properties of multimode BGS, we plot the BGS for the intramodal gain of the fundamental mode (FM) (mode number $m=1$) and a higher-order mode (HOM) (mode number $m=120$), as well as the intermodal gain between them, in Fig. 3(a). The intramodal gain for the FM (solid red curve) has the maximum peak value. The intramodal gain for the HOM (dash-dotted blue curve) has a slightly lower peak value, due to a larger effective acousto-optic area [3,83] and also shows secondary peaks corresponding to interactions with higher-order acoustic modes. Interestingly, the intermodal gain (dashed black and yellow curves) between the FM and the HOM has a substantially lower peak value than both intramodal curves. This is a result of inefficient acousto-optic overlap between the FM and the HOM due to significant variations in the polarization and intensity profile (shown in the inset). Furthermore, the intermodal BGS (dashed black and yellow curves) peak at a higher Brillouin frequency than the intramodal BGS (solid red and dash-dotted blue curves). This is because lower-order radially symmetric acoustic modes facilitate intramodal gain, whereas higher-order acoustic modes (with higher eigenfrequency) are

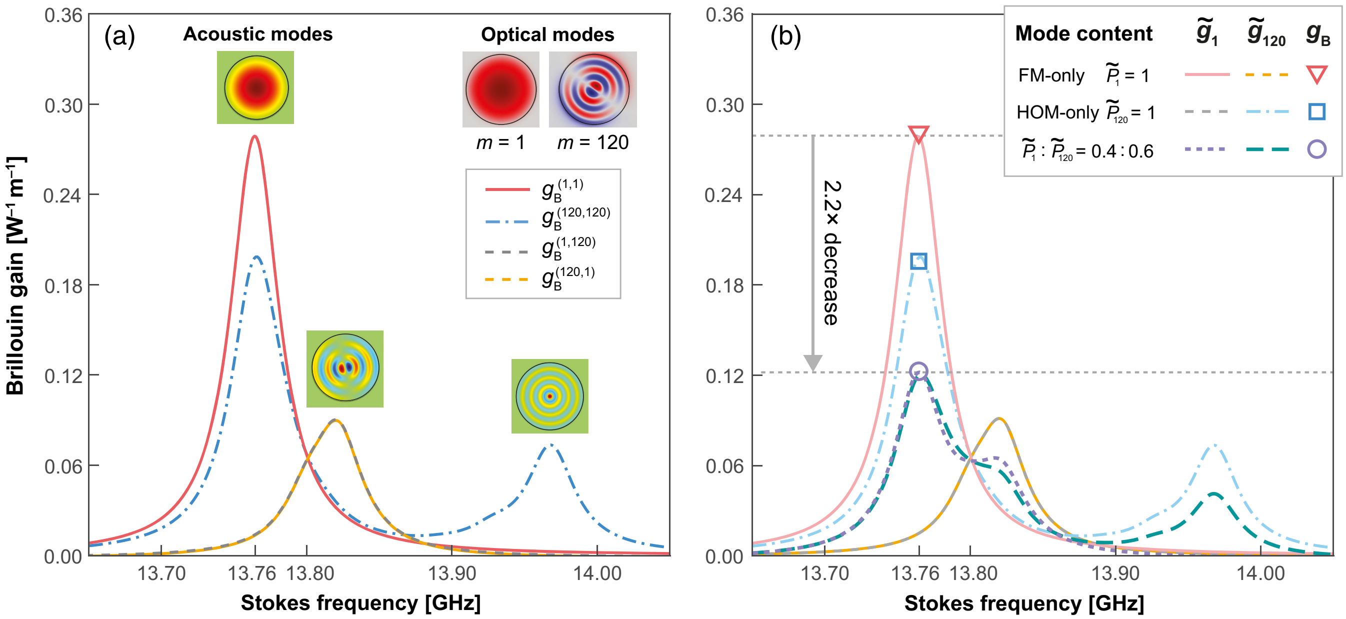

FIG. 3. Illustration of SBS suppression with multimode excitation using a two-mode example. (a) Brillouin gain spectra (BGS) for a circular step index fiber (fiber A) (summed over all possible acoustic interactions) for the fundamental mode (FM) ($m = 1$) and a higher-order mode (HOM) ($m = 120$). The intermodal BGS (dashed black and yellow curves, remains identical under index interchange) have significantly lower peak values and relatively higher Brillouin frequency (frequency of the peak) compared to both intramodal BGS (solid red and dash-dotted blue curves). Acoustic modes with dominant contributions are shown corresponding to each peak in the BGS. The intramodal BGS has a dominant contribution from the fundamental acoustic mode, whereas the intermodal BGS has a dominant contribution from the higher-order acoustic mode. As shown, intramodal BGS for HOMs can have multiple peaks. (b) Effective BGS in the FM and HOM Stokes modes for three different input excitations. For single-mode input excitations (FM-only or HOM-only), the effective BGS in each mode $\tilde{g}_m$ is given by the corresponding intramodal or intermodal BGS [curves reproduced in (b) with lighter colors]. For a multimode excitation, the effective BGS in each Stokes mode is a weighted sum of intramodal and intermodal BGS (shown as dotted purple and long-dashed teal curves for optimal two-mode excitation). The overall Brillouin gain coefficient g_B for a particular input excitation is given by the maximum value of effective BGS across all the Stokes modes and frequencies [Eq. (27)]. g_B is highest for FM-only excitation (red triangle), is 1.4 times lower for HOM-only excitation (blue square), and is 2.2 times lower for optimal combination (purple circle) of FM and HOM ($\tilde{P}_1 \approx 0.4$ and $\tilde{P}_{120} \approx 0.6$). Thus, SBS threshold (which is inversely proportional to g_B) is 2.2 times higher for optimal two-mode excitation compared to FM-only excitation. Further power division among many modes leads to even higher SBS thresholds.

responsible for intermodal gain. We show the profile of the acoustic modes with the dominant contribution corresponding to each of the peaks in the BGS in Fig. 3(a).

The relatively lower peak value of intermodal BGS along with the shifted spectrum suggests that multimode excitation can lead to SBS suppression by lowering the effective Brillouin gain [Eq. (21)], leading to a higher SBS threshold. To show this explicitly, we consider three different input excitations: (i) all of the signal power is in the FM ($m = 1$)—this will be used as a reference since this is by default the case in single mode fibers (SMFs); (ii) all of the signal power is in a single HOM ($m = 120$); and (iii) the signal power is divided between the FM and HOM. The SBS threshold is inversely proportional to the overall Brillouin gain coefficient g_B [Eq. (26)], which is given by the maximum value of the effective BGS across all the Stokes modes and frequencies [Eq. (27)]. Recalling that the effective Brillouin gain is a weighted combination (depending on the input signal mode content) of pairwise BGS [see Eq. (21)], we can compare the three cases. When all of the power is in a single mode, as in cases (i) and (ii), the effective BGS is simply equal to the intramodal BGS for that mode, $g_B^{m,m}$, and the intermodal BGS $g_B^{n,m}$ for modes $n \neq m$. Typically, we find that intramodal BGS have a higher peak value than intermodal BGS. Hence, for single-mode excitations g_B is simply the peak value of respective intramodal BGS shown in Fig. 3(a), which we reproduce in Fig. 3(b) (solid red and dash-dotted blue curves). Since the FM-FM BGS has the highest peak value [red triangle in Fig. 3(b)], FM-only excitation results in the lowest SBS threshold (for reference, we denote it by P^0_{th}). The HOM-only curve has a slightly lower peak [blue square in Fig. 3(b)] and leads to a higher SBS threshold ($1.4P^0_{\mathrm{th}}$). In case (iii) (two-mode excitation), the effective BGS in each Stokes mode is a weighted sum of intramodal and intermodal BGS [shown as dotted purple and long-dashed teal curves in Fig. 3(b)]. Maximum peak value g_B in this case can be 2.2 times lower [purple circle in Fig. 3(b)] for the

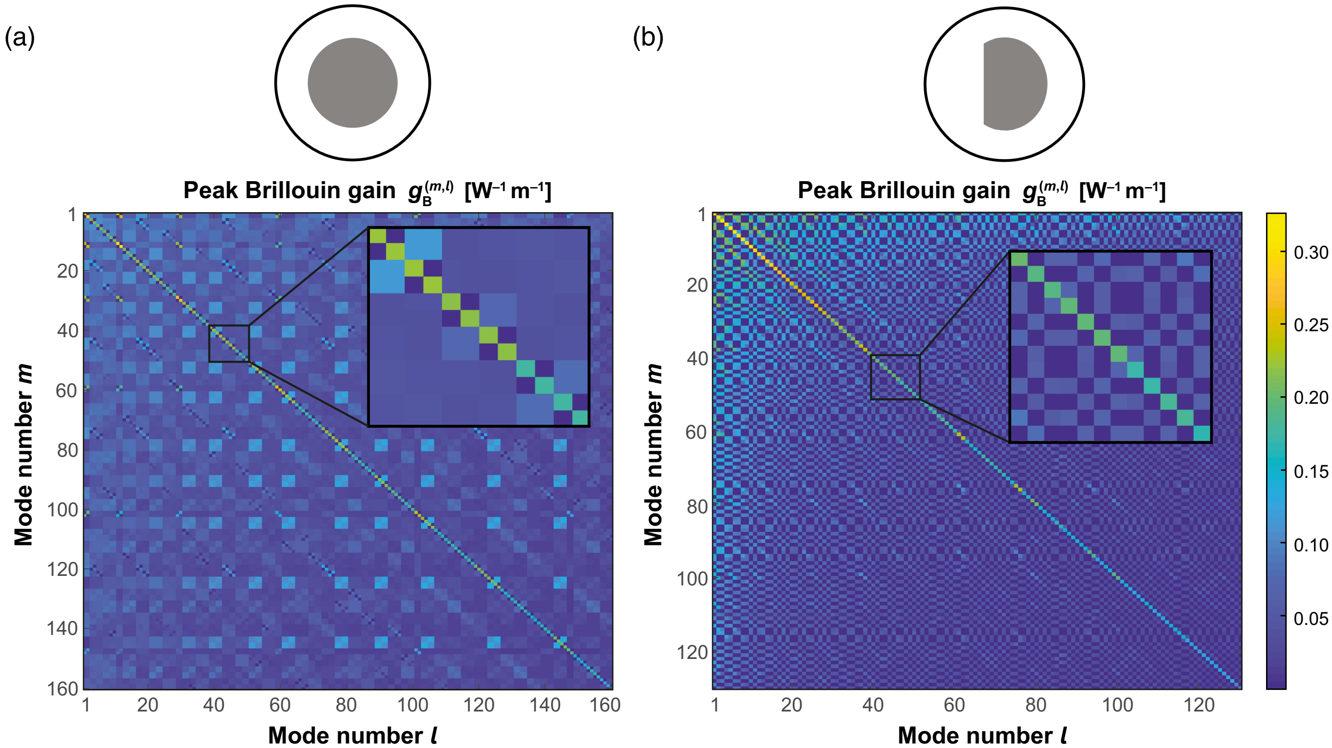

FIG. 4. Matrix of peak values of pairwise BGS for all possible Stokes-signal mode pairs for highly multimode step-index fibers with (a) circular (fiber A) and (b) D-shaped (fiber B) cross sections. The insets show enlarged views of sections of the matrices in each case. The modes are ordered according to their effective refractive indices. The peak values of intermodal BGS (off-diagonal elements) are typically lower than the intramodal BGS (diagonal elements) for both fibers A and B. The matrix for fiber B has a checkerboard structure, since modes are either completely x or y polarized. Fiber A does not exhibit this structure due to the spatially varying polarization patterns of the optical modes.

optimal combination of FM and HOM ($\tilde{P}_1 \approx 0.4$ and $\tilde{P}_{120} \approx 0.6$), leading to a 2.2× higher SBS threshold compared to FM-only excitation. Note that for this two-mode case the optimal power distribution corresponds to matching the two peak values of the effective BGS for the FM and HOM.

The SBS suppression (increase in SBS threshold) illustrated with two modes ($m = 1$ and $m = 120$) in Fig. 3 is due to generic properties of BGS such as relatively weaker intermodal gain and shifted BGS peaks and, hence, generalizes to many-mode excitation. In Fig. 4(a), we show in a color scale the matrix of peak values of BGS for all possible mode pairs for the circular step-index fiber described before (fiber A). This gives a 160×160 matrix of positive entries, where each element (m, n) describes the SBS interaction between Stokes mode m and signal mode l. An enlarged view of a section of the matrix is shown in the inset. It can be clearly seen that the intermodal gain (off-diagonal elements) is generically smaller than the intramodal gain (diagonal elements). For generality, we also consider another fiber (fiber B), which has all the same material properties as fiber A but with a D-shaped cross section (see Fig. 2). A motivation to study this fiber is the ray chaotic nature of the D-shaped cavities, leading to more ergodic modal profiles. This fiber supports 130 optical modes with polarization roughly aligning with either the x axis (axis of symmetry) or y axis (perpendicular to x axis), unlike the circular cross-section fiber (see Fig. 2). The matrix of peak values of the BGS for fiber B is shown in Fig. 4(b). An enlarged view of a section of the matrix is shown in the inset. The intermodal gain is again generically weaker than the intramodal gain, similar to fiber A. In addition, there is a checkerboard pattern in the matrix which is a result of complete decoupling of modes with two orthogonal polarizations (x and y). The contrast between intermodal and intramodal gain (for modes with the same polarization) is actually found to be lower than for fiber A.

The presence of relatively weaker intermodal gain in both circular and D-shaped fiber suggests that exciting multiple modes instead of exciting only the FM or a single HOM can lead to substantially higher SBS threshold. To show this, we consider equal division of signal power in all of the modes up to mode number M_e and calculate the SBS threshold as M_e is varied. The results for fiber A are shown in Fig. 5(a). For reference, we compare all the results to the SBS threshold for FM-only excitation (dashed black line) by defining a threshold increase factor as the ratio of the SBS threshold for a given excitation divided by that with

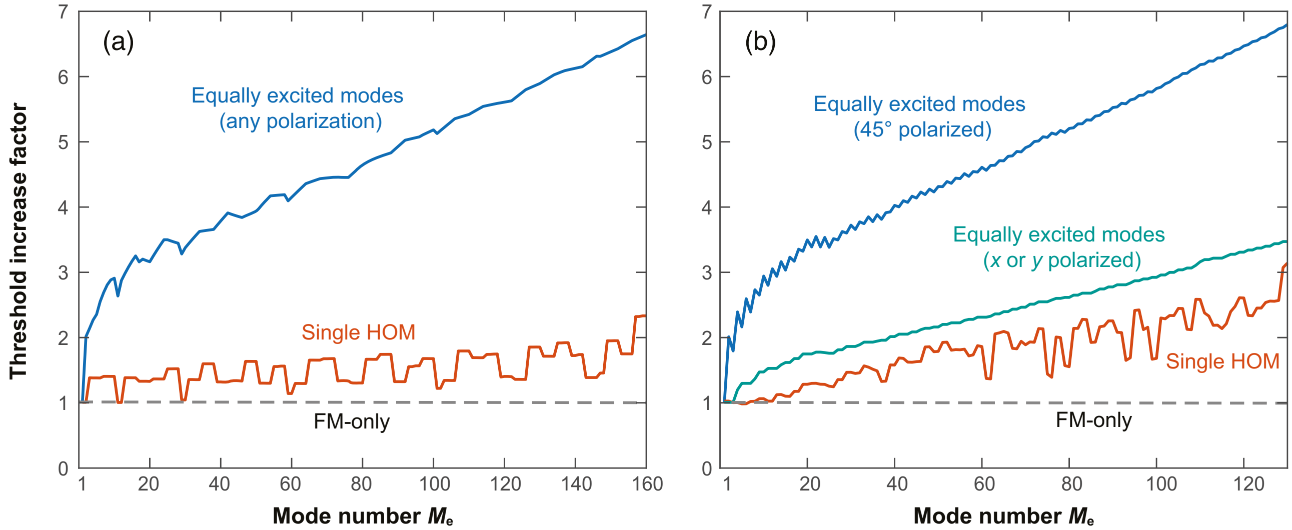

FIG. 5. Scaling of the SBS threshold with the number of modes for different input excitations in multimode step index fibers with (a) circular (fiber A) and (b) D-shaped (fiber B) cross sections. For reference, the FM-only excitation is set to be 1, shown as a black dashed line. In (a), the blue curve represents the case when all the modes are equally excited up to mode number M_e with any polarization. When $M_e = 160$, a 6.5-times-higher SBS threshold is obtained for equal mode excitation, substantially higher than exciting a single HOM (mode number $= M_e$) shown by the orange curve. In (b), the SBS threshold for equal mode excitation increases more slowly for x- or y-polarized input (teal curve) as compared to input polarized at 45° (blue curve) with respect to the axis of symmetry (x axis). A 6.7-times-higher SBS threshold is obtained when $M_e = 130$ for equal mode excitation and 45° polarization, significantly higher than exciting a single HOM (mode number $= M_e$) shown by orange curve.

FM-only excitation. The SBS threshold increases almost monotonically for equal mode excitation (solid blue curve) as M_e is increased and reaches 6.5 times when $M_e = 160$. As illustrated with the two-mode example above, the increase in SBS threshold upon multimode excitation results from relatively small intermodal gain and not simply from increasing the acousto-optic effective area, due to increasing mode order. To illustrate this further, we also show in the plot the SBS threshold when the highest single HOM (mode number = M_e) is excited (orange curve). For the best HOM ($M_e = 160$), the threshold increase is 2.1 times, significantly lower than for equal mode excitation. As we note above, power division tends to broaden the effective SBS gain spectrum, which also reduces the peak value. This is seen dramatically in the case of equal power division among all 160 modes of this circular fiber. The effective gain spectrum is shown in Fig. 6, compared to that of FM-only excitation. We find a more than doubling of the gain bandwidth under equal power division, along with the peak value of the spectrum decreasing greatly, leading to a factor of 6.5 increase in the SBS threshold.

The threshold behavior for fiber B, shown in Fig. 5(b), has an interesting new feature. For the D-shaped fiber core, the SBS threshold strongly depends on the input polarization. When the polarization of light is along either the x or y axis, and power is equally divided in the modes (teal curve), the maximum SBS threshold obtained is 3.5 times higher than the FM-only threshold for $M_e = 130$. However, with polarization at an angle of 45° to the x axis, the maximum SBS threshold is 6.7 times higher than FM-only excitation,

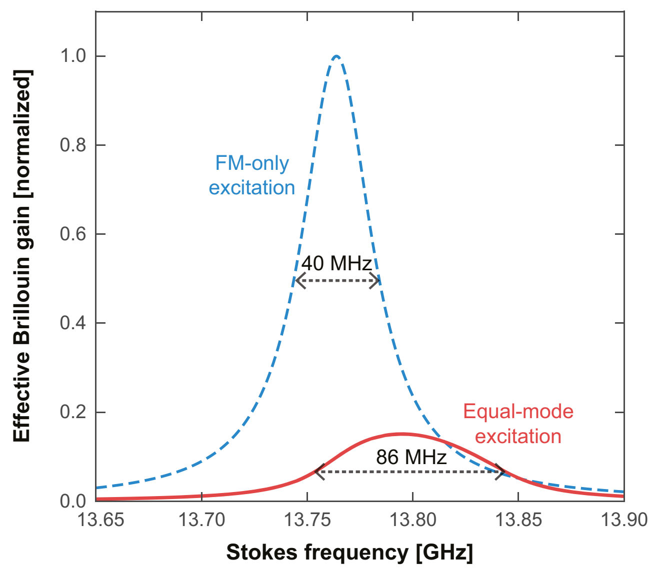

FIG. 6. Effective Brillouin gain spectra in fundamental Stokes mode for FM-only excitation (dashed blue curve) and 160-equal-mode excitation (solid red curve) in a circular step index fiber (fiber A). The spectra are normalized such that peak value of gain for FM-only excitation is equal to one. Brillouin gain for equal mode excitation is significantly broadened leading to a full width at half maximum (FWHM) of 86 MHz, which is more than twice the FWHM for Brillouin gain for FM-only excitation (40 MHz). The broadening is a result of addition of multiple intermodal and intramodal BGS which peak at different frequencies, upon equal mode excitation. As a result of this broadening and weak intermodal coupling, the peak value of Brillouin gain is 6.5 times lower for equal mode excitation, leading to an equivalent increase in SBS threshold.

when all 130 modes are equally excited (blue curve). A strong dependence of SBS threshold on input polarization has been previously observed in single-mode birefringent fibers [84]. Similar dependence has been observed for the threshold of transverse mode instability [85], which is a thermo-optic nonlinear effect that results from a four-wave mixing type interaction, similar to SBS. In our model, it is easy to understand this dependence through the checkerboard structure of the BGS matrix [see Fig. 4(b)]. When the light is launched at 45°, power is launched equally in x- and y-polarized modes, which have zero intermodal interaction with each other, qualitatively reducing the intermodal gain, leading to roughly a factor of 2 reduction in the total effective SBS gain and almost a twofold increase in SBS threshold. Note that this polarization dependence is not present in fiber A (circular core), since there is no preferred axis of symmetry in an ideal circular fiber. Overall results in both the circular and D-shaped fibers show that a significant enhancement (approximately 6.5) in SBS threshold can be obtained upon equal excitation of many modes.

V. DISCUSSION AND CONCLUSION

In this work, we have presented and implemented the first accurate theoretical model for predicting the SBS threshold under arbitrary multimode excitation. The theory elucidates the physics of intermodal gain and explains why it is generically weaker than intramodal gain, hence favoring highly multimode excitation to achieve a substantially higher SBS threshold. The theory presented above can be used, after the applicable approximations (primarily, the assumptions of undepleted signal and phase matching), to calculate the SBS gain spectrum and threshold for highly multimode fibers with any refractive index profile and cross-sectional geometry, taking into account fully the vector nature of the optical fields and forces. The signal modal power distribution enters the theory as a set of control parameters, determining the effective spectrum and the threshold. The vector nature of optical forces considered here is necessary to obtain an accurate theory of SBS for highly multimode excitations. In Appendix A, we generalize the formalism in the main text to include the tensor nature of the acousto-optic interaction. The generality of our linearized equations, with correct treatment of vector modes and tensor interaction coefficients, makes them suitable for micro- and nanowaveguides, although in the latter case boundary terms [17,30,69] will need to be added to the sources, which will modify the overlap integrals. These equations are potentially applicable in semiconductor waveguides, where shear waves play a significant role.

As demonstrated, these equations provide a realistic computational framework for calculating the intramodal and intermodal gain spectra for all pairs of modes in a highly multimode fiber. The power in each Stokes mode grows exponentially, with a modal growth rate independent of the power in the other Stokes modes. Typically, the SBS threshold will be determined by the mode with the highest growth rate, and each growth rate depends strongly on the modal power distribution of the signal excitation. We have shown that dividing the input power among modes generically decreases the maximal Stokes gain, increasing the SBS threshold, due to the relative weakness of the intermodal gain, and the broadening of the effective SBS spectrum.

While our formalism includes effects neglected in previous theories, we are not able to compare our results to exact numerical simulations, since they are impractical due to the multiscale nature of the problem. In parallel with this theoretical work, experiments have been performed on SBS in passive multimode fibers with results in quantitative agreement and confirming the basic physical principle implied by our theory: that exciting a multimode fiber with many modes substantially increases the SBS threshold compared to single-mode excitation of the same fiber [28]. One important prediction of the current theory, not studied here, is that the increase of the SBS threshold is independent of the relative *phases* of the signal modal amplitudes and depends on only the power in each mode. This suggests that these relative phases can be controlled (e.g., using an SLM), so as to refocus the beam at the output, while maintaining an increased SBS threshold due to multimode excitation. The experiments validated this important property, demonstrating refocusing of the speckled multimode beam to a reasonable focal spot in the far field using wavefront shaping at the input [28]. Further applications of the theory to experimental data under different excitation conditions are made in that work as well.

In the current work, we have presented only results for single-mode and equal mode excitation of a fiber. Beyond this, our theoretical framework allows us to pose the maximization of the SBS threshold as a convex optimization problem for a given matrix of Brillouin gain coefficients. In future work, we will explore this approach and expect that an even larger suppression of SBS can be achieved with a highly multimode, but nonuniform input signal power distribution [86].

Suppression of SBS is especially important in fiber amplifiers, since it will allow power scaling in narrow-linewidth high-power fiber lasers [22]. In this work, we have not explicitly included the signal gain of the active fiber. This is trivial in the absence of linear mode-dependent gain and loss [87], but to model realistic fiber amplifiers these effects will need to be included. This can be modeled and/or measured and included without significant complication of the analytic and computational framework. Similarly, linear mode coupling due to fiber bending or other fiber imperfections and external perturbations can be a significant effect in realistic fibers. Our formalism allows taking this into account straightforwardly by replacing the fractional signal power in each mode at the input $\tilde{P}_l$ in

Eq. (27) with fractional signal power in each mode averaged over the length of the fiber $\langle \tilde{P}_l \rangle_z$. For a multimode fiber with random but time-invariant microbends, linear mode coupling can be modeled as successively multiplying the signal mode content vector by banded random matrices [88]. The polarization mixing is already accounted for in the coupling of vector modes of the fiber. This approach allows calculating averaged mode content $\langle \tilde{P}_l \rangle_z$ via numerical integration.

A further quite important effect in fiber amplifiers is that of gain saturation of the signal [89]. This is a space-dependent nonlinear effect which cannot be neglected if one wants to describe such systems quantitatively. However, we can still neglect the depletion of the signal to the Stokes mode when calculating the saturated signal field; moreover, there are iterative self-consistent approaches to include this in a semianalytic framework [90]. The qualitative physics which makes intermodal gain weaker than intramodal gain and favors highly multimode excitation is not changed by gain saturation.

Increasing the threshold for SBS is very important for the long-range optical transmission [91], which is limited by backscattering. Note that the random coupling of fiber modes can scramble the optical signals, but the information is not lost, as long as the mode coupling is a linear and deterministic process. Even for a long fiber, the relation between the input fields in all modes and output fields in all modes is completely characterized by the transmission matrix of the fiber, $E_{\rm out} = TE_{\rm in}$ at any frequency. Coherent measurement of output fields in all modes allows full recovery of the input fields, which has already been done in recent years [92]. In the case of optical pulses, there can be broadening by modal dispersion in a fiber, but again this can be digitally compensated to recover the optical signals by digital signal processing (DSP) with frequency-resolved or time-resolved transmission matrix. In fact, coherent communication protocol based on multi-input, multi-output was already developed for mode-division multiplexing in telecommunications, thanks to the rapid progress of DSP [93,94].

Another important application of SBS in fibers has been in developing distributed sensors for temperature and strain. Most studies focus on single-mode fibers, but it has been posited that SBS in multimode fibers can lead to better performance in sensing applications [95]. In MMFs, different Stokes modes have distinct Brillouin frequency shifts, which also depend on external parameters such as temperature and strain. Thus, sensing platforms based on SBS in MMFs can possibly be utilized to extract more information about the fiber environment compared to SMFs. Our multimode SBS theory will be quite useful in providing a comprehensive framework for any such future studies.

Finally, our general approach is applicable to model other nonlinear effects for which wavefront shaping and modal control can be applied to affect their manifestation. Already we have applied this theoretical approach to the study of transverse modal instability and uncovered new physical effects due to the thermal origin of the instability [51]. In this case, multimode excitation is predicted to be even more effective in suppressing the instability. A similar approach seems possible for controlling the effect of Kerr nonlinearity in multimode fibers [96,97]. In our view, wavefront shaping in multimode fibers has the potential to become a standard tool to control nonlinear effects in fibers, and possibly in waveguides, of great practical utility.

ACKNOWLEDGMENTS

This work is supported by the Air Force Office of Scientific Research (AFOSR) under Grants No. FA9550-20-1-0129, No. FA9550-20-1-0160, and No. FA9550-24-1-0182. K. W. is supported by a grant from Simons Foundation. S. C. W. is supported by an Australian Research Council (ARC) Future Fellowship (FT200100154). We thank Heike Ebendorff-Heidepriem, David J. Ottaway, Ori Henderson-Sapir, Shuen Wei at University of Adelaide, Linh V. Nguyen at University of South Australia, and Peter Rakich and Owen D. Miller at Yale University for helpful technical discussions. We also thank Yale University and the University of Adelaide for providing computational resources.

APPENDIX A: GENERALIZED ACOUSTO-OPTICAL INTERACTION

1. Optical equation

In the main text, we study isotropic silica fibers, where acousto-optical interaction can be accurately described by interaction between vector electric fields and scalar acoustic fields. In general, however, the acousto-optical interaction takes a more complicated form, involving a fourth-rank photoelastic tensor coupling a vector electric field to a vector acoustic displacement field. The formalism for multimode SBS threshold developed in the main text can be utilized for the tensor acousto-optical interactions by replacing the overlap integral in Eq. (22) with an appropriately generalized formula. In this section, we provide the generalized formula for the overlap integral and show that it reduces to the form in Eq. (23) under suitable approximations valid for standard silica fibers. The presence of shear effects also requires a generalized acoustic equation involving elasticity and viscosity tensors, which is discussed in the next subsection.

The generalized nonlinear polarization due to photoelastic effect is given by the tensor product of the second-rank susceptibility tensor $\overleftrightarrow{\chi}_N$ and the electric field [68,69]:

$$\vec{P}_{\rm NL} = \overleftrightarrow{\chi}_N \cdot \vec{E}, \qquad \overleftrightarrow{\chi}_N = \overleftrightarrow{\pi} : \nabla \otimes \vec{u} = \overleftrightarrow{\pi} : \overleftrightarrow{S}. \qquad \text{(A1)}$$

Here, $\otimes$ denotes the outer product of two vectors and $(\nabla \otimes \vec{u})_{ij} = \partial_i u_j \equiv \overleftrightarrow{S}_{ij}$ is the second-rank strain tensor. $\overleftrightarrow{\pi} : \overleftrightarrow{S} = \sum_{kl} \pi_{ijkl} S_{kl}$ denotes the contraction of the strain tensor with the fourth-rank photoelastic tensor $\overleftrightarrow{\pi}$ to yield the second-rank susceptibility tensor $\overleftrightarrow{\chi}_N$. The photoelastic tensor generalizes the electrostriction constant γ_e used in the main text.

As such, the overlap integral in Eq. (15) corresponding to the optical source term is generalized to the following form:

$$O_2 = \langle [(\overleftrightarrow{\pi} : \vec{q}^* \otimes \vec{u}_k^{ml*}).\vec{f}_l^{(1)}].\vec{f}_m^{(2)*}\rangle. \quad (A2)$$

Here, $\vec{u}_k^{ml*}$ is the vector displacement field of the kth acoustic mode, driven by the interference of optical modes m and l and $\vec{q} = \nabla_T - iq_{ml}\hat{z}$. The derivative of the acoustic mode profile, $\vec{u}_k^{ml*}$, contracted with the photoelastic tensor $\overleftrightarrow{\pi}$, gives the nonlinear susceptibility, which, when multiplied with optical mode profile $\vec{f}_l^{(1)}$, gives the acousto-optic polarization field. The projection of this polarization on the particular Stokes mode profile, $\vec{f}_m^{(2)}$, gives the optical scattering strength.

For elastically isotropic fibers, the full photoelastic tensor can be described by just two independent constants [72,75,98], resulting in dramatic simplification in the form of the overlap integral. The form of $\overleftrightarrow{\pi}$ for an isotropic medium can be written in the index notation as follows:

$$\pi_{ijkl} = \pi_{1122}\delta_{ij}\delta_{kl} + \pi_{1212}(\delta_{ik}\delta_{jl} + \delta_{il}\delta_{jk}), \quad (A3)$$

where π_{1122} and π_{1212} are the two independent parameters describing the entire photoelastic tensor and δ_{ij} is the Kronecker delta function for indices i and j. A useful way to visualize $\overleftrightarrow{\pi}$ in this case is by employing the Voigt notation [99,100]. We introduce a set of six new labels for the three diagonal and the three independent off-diagonal elements: $\{1,2,3,4,5,6\} \equiv \{11,22,33,12,13,23\}$. With such notation, the fourth-rank tensor $\overleftrightarrow{\pi}$ can be written as the following 6×6 matrix [100]:

$$\overleftrightarrow{\Pi} = \begin{bmatrix} \pi_{12}+2\pi_{44} & \pi_{12} & \pi_{12} & 0 & 0 & 0 \\ \pi_{12} & \pi_{12}+2\pi_{44} & \pi_{12} & 0 & 0 & 0 \\ \pi_{12} & \pi_{12} & \pi_{12}+2\pi_{44} & 0 & 0 & 0 \\ 0 & 0 & 0 & \pi_{44} & 0 & 0 \\ 0 & 0 & 0 & 0 & \pi_{44} & 0 \\ 0 & 0 & 0 & 0 & 0 & \pi_{44} \end{bmatrix}. \quad (A4)$$

The π_{12} component (π_{1122} in original notation) is directly related to the electrostriction constant γ_e. The formula for $\overleftrightarrow{\pi}$ in Eq. (A3) can be substituted in Eq. (23) to simplify the overlap integral for the elastically isotropic materials. We contract $\overleftrightarrow{\pi}$ and $\vec{f}_l^{(1)} \otimes \vec{f}_m^{(2)*}$ to obtain

$$\begin{aligned} O_{mlk} = {} & \pi_{12}\langle \vec{\nabla}(\vec{f}_l^{(1)} \cdot \vec{f}_m^{(2)*}) \cdot \vec{u}_k^{ml*}\rangle \\ & + 2\pi_{44}\langle \vec{\nabla} \cdot (\vec{f}_l^{(1)} \otimes \vec{f}_m^{(2)*}) \cdot \vec{u}_k^{ml*}\rangle. \end{aligned} \quad (A5)$$

The overlap integral contains two terms, one for each of the two independent components of $\overleftrightarrow{\pi}$. Here, $\vec{\nabla}$ is equal to $\vec{\nabla}_T - iq_{ml}\hat{z}$. We can further simplify the first term in the overlap integral by using integration by parts:

$$\begin{aligned} O_{mlk} = {} & \pi_{12}\langle \vec{f}_l^{(1)} \cdot \vec{f}_m^{(2)*}\vec{\nabla} \cdot \vec{u}_k^{ml*}\rangle \\ & + 2\pi_{44}\langle (\vec{\nabla} \cdot \vec{f}_l^{(1)})\vec{f}_m^{(2)*} \cdot \vec{u}_k^{ml*}\rangle \\ & + 2\pi_{44}\langle (\vec{f}_l^{(1)} \cdot \vec{\nabla})\vec{f}_m^{(2)*} \cdot \vec{u}_k^{ml*}\rangle. \end{aligned} \quad (A6)$$

The first term in the overlap integral (we call it the direct interaction term) is proportional to π_{12} and the dot product between the Stokes and the signal mode profiles multiplied with the divergence of the displacement field profile. The other two terms (we call them cross interaction terms) consist of dot products between the optical mode and displacement field profiles multiplied with the derivative of the remaining optical mode profile. Typically, the direct interaction term is significantly larger than the cross interaction terms. This is due to the predominantly transverse nature of the optical modes [77,78] and longitudinal nature of the acoustic modes [31,73,81], which leads to an extremely small dot product between optical and acoustic mode profiles. Therefore, we can ignore the cross interaction terms leading to

$$O_{mlk} \approx \pi_{12}\langle \vec{f}_l^{(1)} \cdot \vec{f}_m^{(2)*}\vec{\nabla} \cdot \vec{u}_k^{ml*}\rangle. \quad (A7)$$

It should be noted that for specialty optical fibers or sufficiently higher-order modes the primarily longitudinal and transverse character of acoustic and optical modes can break down, leading to nontrivial contribution from the cross interactions, in which case Eq. (A6) should be used for accurate calculations.

2. Acoustic equation

Similar to the optical equation, the source term in the acoustic equation takes a generalized form involving the photoelastic tensor. In addition, for the acoustic equation, the wave operator also generalizes leading to the following equation [17,68,69]:

$$\left[\nabla \cdot \left(\overleftrightarrow{C} + \frac{\partial}{\partial t}\overleftrightarrow{\eta}\right) : \nabla \otimes -\rho_0 \frac{\partial}{\partial t^2}\right]\vec{u} = -\vec{F}, \quad (A8)$$

where $\overleftrightarrow{C}$ and $\overleftrightarrow{\eta}$ are fourth-rank elasticity and viscosity tensors, respectively [73,74]. The elasticity tensor generalizes various elasticity moduli which determine the acoustic velocities in the fiber. The viscosity tensor plays the role of generalized phonon loss in the fiber. The source term $\vec{F}$ is the optical force, given by [69]

$$\vec{F} = -\frac{1}{2}\nabla \cdot [\overleftrightarrow{\pi} : \vec{E} \otimes \vec{E}]. \tag{A9}$$

As a result, the overlap integral in Eq. (10) corresponding to the acoustic source term takes the following form:

$$O_1 = -\langle (\vec{q} \cdot [\overleftrightarrow{\pi} : \vec{f}_i^{(1)} \otimes \vec{f}_j^{(2)*}]) \cdot \vec{u}_k^{ij*} \rangle. \tag{A10}$$

The angular brackets $\langle . \rangle$ denote integration over the entire fiber cross section, and $\vec{q}$ is the gradient operator with z component set equal to $-iq_{ij}\hat{z}$. The derivative of the tensor product of optical mode profiles, $\vec{f}_i^{(1)}$ and $\vec{f}_j^{(2)}$, contracted with the photoelastic tensor $\overleftrightarrow{\pi}$, represents the optical force. This is then projected onto the relevant acoustic mode profile $\vec{u}_k^{ij}$ and integrated over the fiber cross section to give the relevant source integral.

Similar to the previous subsection, for isotropic fibers, the acoustic overlap integral can be simplified, and it reduces to a similar form as Eq. (A7). In addition, the elasticity tensor $\overleftrightarrow{C}$ can be described by just two independent constants and takes the following form [73,101]:

$$C_{ijkl} = \lambda\delta_{ij}\delta_{kl} + \mu(\delta_{ik}\delta_{jl} + \delta_{il}\delta_{jk}), \tag{A11}$$

where λ and μ are the well-known Lamé parameters [73,101] and are related to the longitudinal velocity V_L and the shear velocity V_s for the acoustic waves; $\lambda = v_L^2\rho_0$ and $\mu = v_s^2\rho_0$, where ρ_0 is the average density of the material. δ_{ij} is Kronecker delta function for indices i and j. This form of the elasticity tensor, $\overleftrightarrow{C}$, can be directly substituted in Eq. (A8) to obtain a simplified acoustic equation for isotropic fibers [31,66,73,81,102]:

$$\left(\rho_0 V_\mathrm{L}^2 + \eta_{11}\frac{\partial}{\partial t}\right)\nabla(\nabla \cdot \vec{u}) - \left(\rho_0 V_\mathrm{s}^2 + \eta_{44}\frac{\partial}{\partial t}\right)\nabla \times \nabla \times \vec{u} - \rho_0\frac{\partial^2}{\partial t^2}\vec{u} = -\vec{F}. \tag{A12}$$

Here, V_L and V_s are the longitudinal and shear acoustic velocities in the fiber, respectively. ρ_0 is the unperturbed fiber density, and η_{11} and η_{44} are the respective components of the viscosity tensor and provide the relevant acoustic loss. Here, the first term is given by the gradient of the divergence of the displacement field and is proportional to the longitudinal acoustic velocity squared. This term is related directly to the density fluctuations, $\delta\rho = \rho_0 \overrightarrow{\nabla} \cdot \vec{u}$; hence, it maps onto the ∇_T^2 term in the scalar acoustic wave equation [1–3,29]. The second term is given by the curl of curl of displacement field and captures the role of the shear forces, parametrized by the shear velocity V_s. This term has no analog in the scalar acoustic wave equation. Typically, in silica fibers the shear acoustic velocity is much smaller than the longitudinal acoustic velocity [103,104]; this results in primarily longitudinal acoustic modes. However, the nonzero shear velocity does produce an observable effect even for these primarily longitudinal acoustic modes because of the shear-longitudinal coupling due to the boundary conditions. We calculate the longitudinal acoustic modes for a circular step-index fiber, with germanium-doped silica core and pure silica cladding, with [Fig. 7(b)] and without the shear term [Fig. 7(a)]. The details of the fiber parameters are given in Table I. Without the shear term, each acoustic mode is characterized by two indices (i, j), and it varies in the radial direction as an ith-order Bessel function (of the first kind) with $j - 1$ zeros in the core and as a cosine or a sine function with i nodal lines in the azimuthal direction. Including the shear-longitudinal coupling leads to a rapidly varying perturbation (small feature size) in addition to the dominant Bessel-like behavior [31,81]. These fast variations are understood [31,81] and are a result of higher shear propagation constants, due to lower shear velocity in the core compared to the longitudinal velocity. Additionally, the effect of the shear term is higher in the higher-order acoustic mode, compared to the fundamental acoustic mode. These variations can, in principle, substantially affect the calculation of the overlap integrals for the acousto-optic interaction, especially for materials with relatively high shear velocities. To show this, we also calculate the acoustic modes of a possible fiber with negative Poisson ratio [105], such that shear velocity is comparable to the longitudinal velocity. The resultant mode profiles are shown in Fig. 7(c), where it can be seen that shear-longitudinal coupling impacts the mode profiles significantly such that modes of scalar acoustic equation are no longer a good approximation for full vectorial modes [106]. Our formalism allows calculation and utilization of full vectorial acoustic modes to calculate BGS in such fibers.

However, for standard silica fibers, we find that the effect of fast variations due to the shear velocity term in the overlap integrals is small and does not change the Brillouin gain spectra significantly (1%–5% error). For this reason, we conclude that using the scalar theory to evaluate the relevant acoustic modes is a useful and accurate approximation. In that case, to calculate the overlap integral in Eq. (A7), we make the substitution $\rho_0 \overrightarrow{\nabla} \cdot \vec{u}_k^{ml} = g_k^{ml}$, where g_k^{ml} is the kth eigenmode (for optical mode pair $\{m, l\}$) of the scalar density fluctuation equation:

$$\left[\nabla_\mathrm{T}^2 + \left(\frac{\Omega_{mlk}^2}{V_L^2} - q_{ml}^2\right)\right] g_k^{ml} = 0. \tag{A13}$$

Here, ∇_T^2 is the transverse Laplacian, Ω_{mlk} is the modal eigenfrequency, and q_{ml} is the acoustic propagation

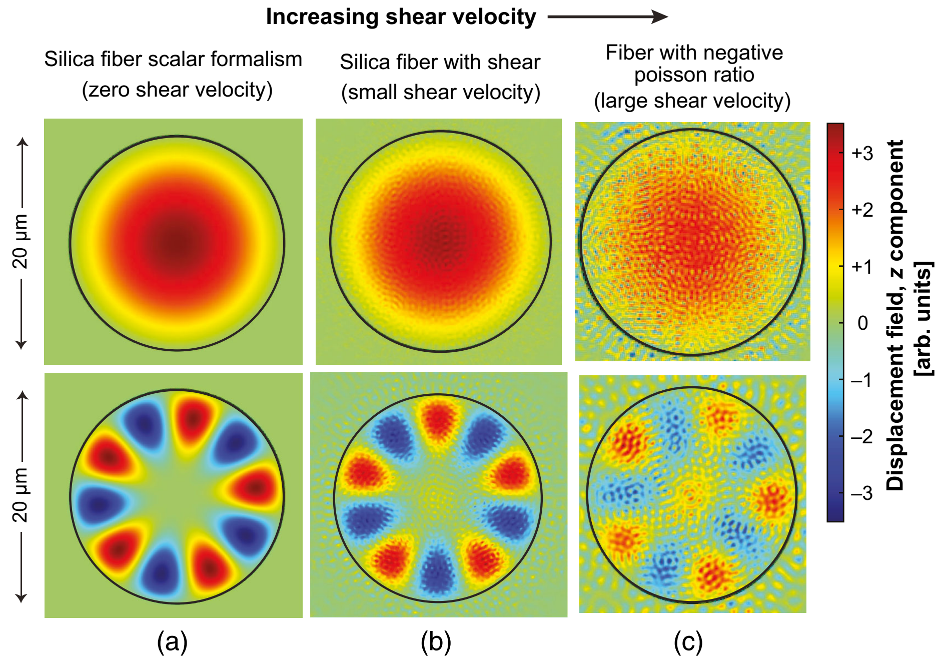

FIG. 7. Mode profiles for the fundamental and higher-order longitudinal acoustic modes, calculated for different regimes of shear velocity for a circular step-index fiber. The fiber is elastically isotropic. (a) When scalar acoustic equation is utilized, where shear velocity is completely neglected, each acoustic mode is characterized by two indices (i, j) and it varies in the radial direction as ith-order Bessel function (of the first kind) with $j-1$ zeros in the core and as a cosine or a sine with i nodal lines in the azimuthal direction. (b) Inclusion of relatively small shear velocity leads to a rapidly varying (small feature size) perturbation in addition to the dominant Bessel-like behavior. In this regime, scalar modes are a good approximation. (c) In a fiber with negative Poisson ratio, where shear velocity is comparable to longitudinal velocity, shear-longitudinal coupling results in significant distortion such that modes of scalar acoustic equation are no longer good approximations for full vectorial modes.

constant in the z direction and is given by $q_{ml} = \beta_l + \gamma_m$. When the scalar acoustic modes are considered, the acousto-optic overlap integral in Eq. (A7) reduces to the formula used in Eq. (23) in the main text:

$$O_{mlk} \approx \langle \vec{f}_l^{(1)} \cdot \vec{f}_m^{(2)*} g_k^{ml*} \rangle. \tag{A14}$$

As stated in Sec. III B, this form of the overlap integral is accurate enough for fibers with relatively low shear velocity. It should be noted that ignoring the shear velocity contribution can lead to substantial errors especially if the shear velocity is comparable or even higher than the longitudinal velocity. In such a case, Eq. (A7) should be used for acoustic mode calculation to evaluate the overlap integrals.

APPENDIX B: COMPARISON TO SCALAR THEORY

In this section, we compare our phase-matched vector multimode SBS theory, simplified for elastically isotropic fibers, to the scalar multimode SBS theory presented in Ke, Wang, and Tang [29] (henceforth referred to as "the scalar theory"). We note that much of the work on SBS in SMFs and in other contexts also uses similar scalar approximations. Ke, Wang, and Tang were able to obtain power growth equations for multimode Stokes growth similar to Eqs. (21) and (22), which are capable of capturing many aspects of the physics of SBS in multimode fibers. However, as we discuss below, the scalar model leaves out effects which have both quantitative and qualitative importance for suppressing SBS in MMF. These authors did not discuss the efficacy of highly multimode excitation in suppressing SBS, nor did they apply it to calculate the full gain matrix for MMFs with many modes (< 100), as we do in the current work. In the scalar theory, SBS growth equations were obtained by solving scalar optical and acoustic wave equations by expanding in terms of scalar linearly polarized (LP) fiber modes and eigenmodes of scalar density fluctuation equation, respectively. This formulation is inadequate for nonisotropic fibers and waveguides, which can have non-negligible contributions from cross components of the photoelastic tensor. Even for isotropic fibers, there can be significant errors due to shear-longitudinal coupling in acoustic modes. However, most importantly, as noted in the main text, the use of uniformly polarized LP modes instead of exact vector fiber modes can lead to overestimation of intermodal gain due to neglect of space-dependent polarization variations in exact fiber modes, which can strongly affect the relevant overlap integrals.

1. Scalar limit of vector theory

There are special cases when the scalar theory is reasonably accurate. An important case is the SBS coupling between forward- (signal) and backward- (Stokes) propagating fundamental modes of the circular step-index fibers. This is by default the case in most SBS studies focusing on single-mode fibers. In this instance, because the vector fundamental mode has constant polarization in space, the scalar multiplication of the amplitudes is the same as the vector dot product between the mode profiles. Another case when scalar theory is accurate is when the cross section of the fiber has two well-defined polarization axes and, therefore, supports uniformly (in space) polarized modes, such as in the case of an elliptical or D-shaped cross section [Figs. 2(c) and 2(d)].

Interestingly, even circular step-index fibers can support uniformly polarized modes, commonly known as linearly polarized (LP) modes. However, these are only approximately the eigenmodes of the fiber, obtained for weakly guiding fibers. Strictly speaking, each LP mode (designated as $\mathrm{LP}_{i,j}$, where i is the azimuthal index and j is the radial index) is a linear combination of two nearly degenerate vector modes $\mathrm{EH}_{i-1,n}$ and $\mathrm{HE}_{i+1,n}$ for $i \geq 1$ [77]. A representative example is shown in Fig. 8(a). The x-polarized $\mathrm{LP}_{7,1}$ mode is equal to $1/\sqrt{2}$ times the sum of exact vector modes $\mathrm{EH}_{6,1}$ and $\mathrm{HE}_{8,1}$. Because the EH and HE modes are not exactly degenerate, there is a small difference, $\Delta\beta$, in their propagation constants. Over short enough length scales ($L \ll 2\pi/\Delta\beta$), the effect of the difference in propagation constants is negligible, and the LP modes form a good basis. In this limit, the scalar theory utilizing the uniformly polarized LP modes should be reasonably accurate. Thus, the effective SBS gain calculated from the scalar and the vector theories is expected to match closely in this limit. This leads to a specific consistency condition on the BGS calculated by the two theories. If all the power is sent in an x-polarized LP mode with mode number m (say, $m = 51$), the effective BGS in that mode according to the scalar theory is given by $g_{\mathrm{scalar}}^{m,m}(\Omega)$. Generically $g_{\mathrm{scalar}}^{(m,l)}(\Omega)$ denotes the BGS for Stokes-signal mode pair (m, l) in the scalar theory. In the vector basis, exciting the x-polarized LP mode with mode number m is equivalent to exciting two vector modes with mode number m and m' with half the power in each mode. Here, m' is the nearly degenerate partner of mode m (for $m = 51, m' = 53$). Therefore, the effective BGS is given by $0.5[g_{\mathrm{vector}}^{(m,m)}(\Omega) + g_{\mathrm{vector}}^{(m,m')}(\Omega)]$. In addition, since in this limit the vector modes are effectively degenerate, there are additional "nontrivially phase-matched terms" (see Sec. III) equal in number to the trivially phase-matched terms, which appear on the off-diagonals of the SBS coupling matrix [Eq. (17)]. This causes the maximum eigenvalue of the matrix to increase by a factor of 2 and minimum eigenvalue to go to zero, with the trace preserved. This is the well-known effect of eigenvalue repulsion in Hermitian matrices due to the off-diagonal elements. Thus, the effective SBS gain in the vector theory is $g_{\mathrm{vector}}^{(m,m)} + g_{\mathrm{vector}}^{(m,m')}(\Omega)$. Hence, the consistency requires

$$g_{\mathrm{scalar}}^{(m,m)}(\Omega) = g_{\mathrm{vector}}^{(m,m)}(\Omega) + g_{\mathrm{vector}}^{(m,m')}(\Omega). \tag{B1}$$

We verify the validity of this relation by explicitly calculating the BGS using both our vector formalism and the scalar theory. As an example, we show the results for $m = 51$ (which gives $m' = 53$) in Fig. 8(b). The individual BGS describing the self- and cross-interaction between m and m' calculated using the vector theory are shown as dotted blue and dashed red curves, respectively. The sum of these curves is given by the solid black curve. The purple dots represent the BGS calculation using the scalar theory which closely matches the sum of the BGS from vector theory (solid black curve), verifying the relation in Eq. (B1).

2. General case: Failure of scalar theory

Note that the scalar theory is valid only in a very special scenario when pairs of exact vector fiber modes are perfectly degenerate. In most experiments, this assumption does not hold true, both due to spatial variation in the propagation constants of the fiber modes which becomes significant in long-enough fibers and due to the presence of disorder. The scalar theory typically overestimates the SBS gain, especially for intermodal SBS couplings, since it simply multiplies the optical mode profiles in the overlap integrals instead of correctly using their spatially varying dot product. This issue is probably the origin of a discrepancy noted but not explained in Table I in Ke, Wang, and Tang [29]. A comparison is presented between the SBS coupling calculated from the scalar theory and the experimental values provided in Ref. [61], showing that the scalar theory consistently overestimates the intermodal gain, while intramodal gain values match closely with the experiments. The vector formalism presented in this work should be more accurate for calculating intermodal coupling and indeed does find weaker intermodal gain than the scalar theory. In general, the inaccuracies in intermodal gain can have significant consequences for the prediction of the SBS threshold upon multimode excitation.

To show this explicitly, we consider exciting fiber A with a diffraction-limited focused spot at the input facet of the fiber for various offset distances d_{in} from the fiber axis. This is a relatively straightforward way of exciting multiple modes with variable mode content in experiments. We plot the prediction of the SBS threshold (relative to FM-only excitation) for each d_{in} using both the vector and scalar formalisms in Fig. 8(c). For $d_{\mathrm{in}} = 0$, only radial modes (with zero azimuthal nodes) are excited leading to a small increase in SBS threshold (1.2 times). As d_{in} is increased, a higher number of nonradial modes are excited, leading to a

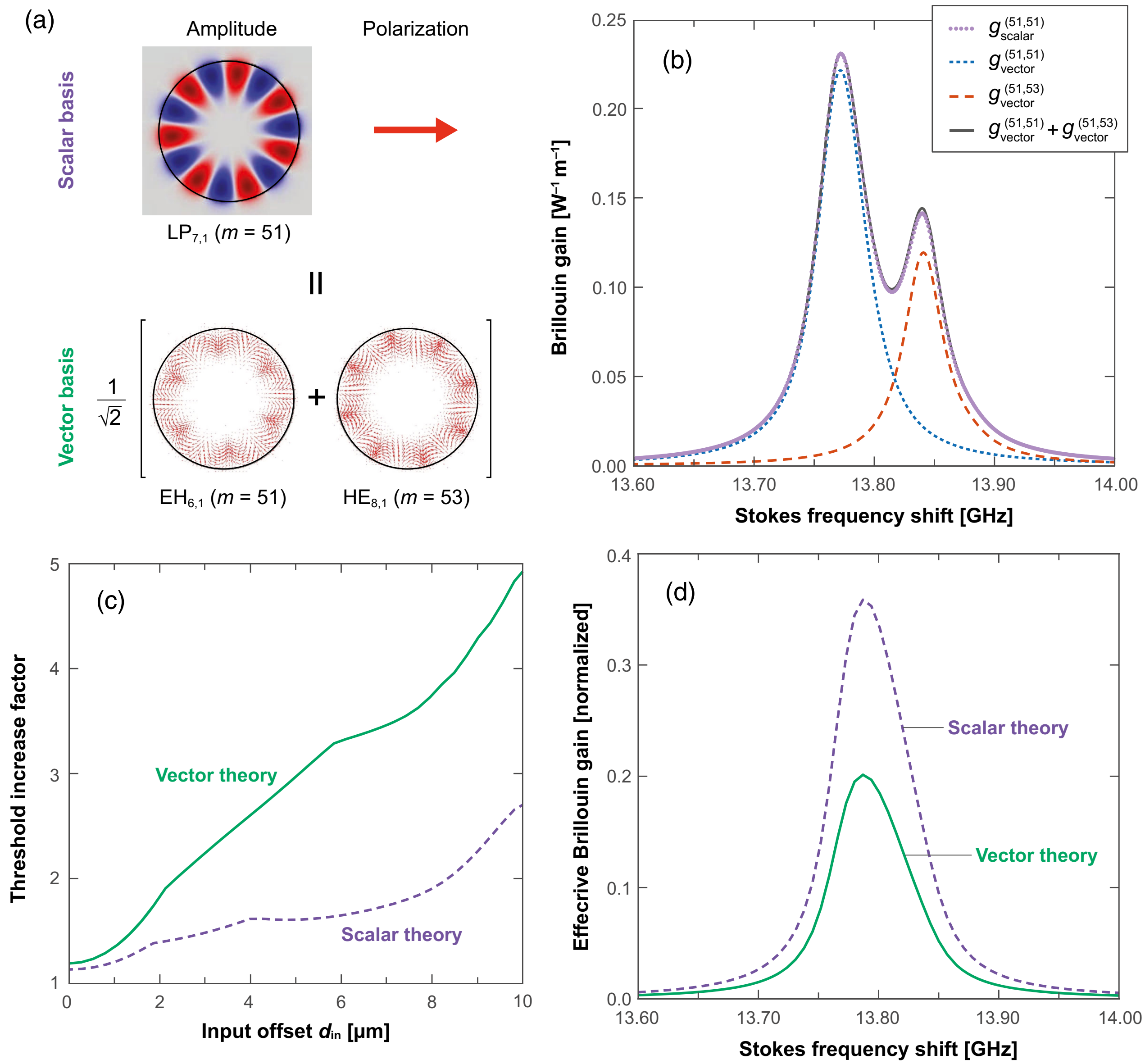

FIG. 8. (a) An example of decomposition of scalar LP modes into exact fiber vector modes. A horizontally (x-) polarized $\mathrm{LP}_{7,1}$ ($m = 51$) mode is an equally weighted linear combination of two nearly degenerate vector modes $\mathrm{EH}_{6,1}$ ($m = 51$) and $\mathrm{HE}_{8,1}$ ($m = 53$). (b) Brillouin gain spectrum (BGS) for various mode combinations calculated using vector and scalar SBS formalism. It shows that intramodal BGS for scalar LP modes (here $\mathrm{LP}_{7,1}$) is equal to the sum of intramodal and intermodal BGS for nearly degenerate vector modes (here $\mathrm{EH}_{6,1}$ and $\mathrm{HE}_{8,1}$) validating the consistency condition in Eq. (B1). This relation is valid only in the limit when vector modes can be considered exactly degenerate, which should not hold for sufficiently long fibers. Comparison of scalar and vector theories: (c) SBS threshold enhancement (w.r.t. fundamental-mode-only excitation) for a focused spot at the input with an offset d_{in} from the fiber axis. As d_{in} is increased, more modes are excited and SBS threshold increases. For real fibers, vector modes are non-degenerate making scalar theory inaccurate, which predicts lower SBS threshold compared to the vector theory. (d) This difference can be seen explicitly by evaluating the effective Brillouin gain spectrum for maximum offset d_{in}, which shows that the scalar theory predicts significantly higher SBS gain due to the overestimation of intermodal gain. Effective gain is normalized to that for fundamental-mode-only excitation.

monotonic increase in SBS threshold. The scalar theory (dashed black curve) consistently predicts lower threshold enhancement than the vector theory (solid red curve) due to the overestimation of intermodal SBS gain. To show this explicitly, we calculate the effective Brillouin gain spectrum for maximum offset, $d_{\mathrm{in}} = 10$ μm, leading to highly multimode excitation. Figure 8(d) shows that the scalar theory predicts significantly higher SBS gain compared to the vector theory. Comparison with recent experiments on SBS in multimode fibers (Fig. 3 in Ref. [28]) confirms that the vector theory is quantitatively accurate, highlighting the impact of the full vectorial formalism presented here.

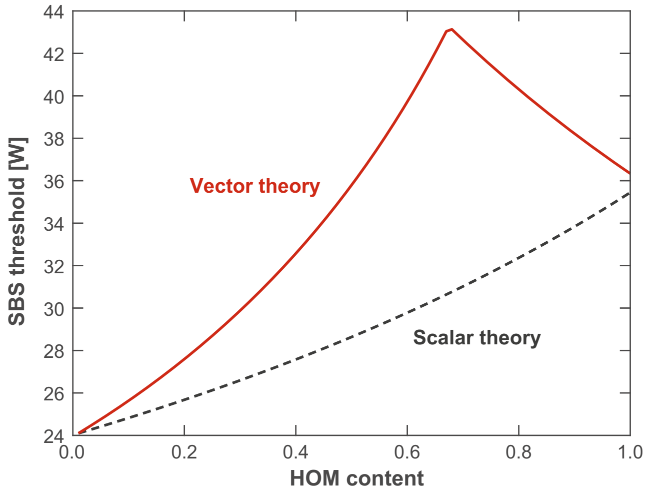

FIG. 9. SBS threshold upon excitation of a combination of fundamental mode ($LP_{0,1}$) and a HOM ($LP_{1,1}$) with variable HOM contents using both the scalar formalism in Ref. [29] and vector SBS formalism developed in our manuscript. The fiber parameters are chosen to match the results of scalar calculation presented in Fig. 4 in Ref. [29]. Our calculations reproduce quantitatively the results of the scalar formalism from Ref. [29] and confirm that the less accurate scalar model predicts monotonically increasing SBS threshold with HOM content, with the highest threshold occurring for single HOM excitation. Our vector model predicts a higher increase in SBS threshold upon power division between the two modes. This discrepancy results from the overestimation of intermodal SBS coupling in the scalar formalism, which neglects polarization mismatch between the two modes.

In fact, for few-mode fibers we find that the scalar formalism can give qualitatively incorrect results. The work of Refs. [29,63] both considered few-mode fibers with two-mode excitation (FM + HOM) and in each case found that the highest SBS threshold is found when exciting only the HOM. However, when we do the calculation with the vector formalism, we find that the highest threshold is for a superposition of FM and HOM weighted toward HOM (see Fig. 9). This is consistent with similar results (for highly MMF) shown in Fig. 5(a).

[1] R. W. Boyd, *Nonlinear Optics* (Academic, New York, 2020).
[2] G. P. Agrawal, *Nonlinear fiber optics*, in *Nonlinear Science at the Dawn of the 21st Century* (Springer, New York, 2000), pp. 195–211.
[3] A. Kobyakov, M. Sauer, and D. Chowdhury, *Stimulated Brillouin scattering in optical fibers*, Adv. Opt. Photonics **2**, 1 (2010).
[4] Z. Bai, H. Yuan, Z. Liu, P. Xu, Q. Gao, R. J. Williams, O. Kitzler, R. P. Mildren, Y. Wang, and Z. Lu, *Stimulated Brillouin scattering materials, experimental design and applications: A review*, Opt. Mater. **75**, 626 (2018).
[5] C. Wolff, M. Smith, B. Stiller, and C. Poulton, *Brillouin scattering—Theory and experiment: Tutorial*, J. Opt. Soc. Am. B **38**, 1243 (2021).
[6] L. Brillouin, *Diffusion of light and x-rays by a homogeneous transparent body*, Ann. Phys. (N.Y.) **9**, 88 (1922).
[7] R. Chiao, C. H. Townes, and B. Stoicheff, *Stimulated Brillouin scattering and coherent generation of intense hypersonic waves*, Phys. Rev. Lett. **12**, 592 (1964).
[8] E. Ippen and R. Stolen, *Stimulated Brillouin scattering in optical fibers*, Appl. Phys. Lett. **21**, 539 (1972).
[9] L. Thévenaz, *Slow and fast light in optical fibres*, Nat. Photonics **2**, 474 (2008).
[10] J. Kim, M. C. Kuzyk, K. Han, H. Wang, and G. Bahl, *Non-reciprocal Brillouin scattering induced transparency*, Nat. Phys. **11**, 275 (2015).
[11] T. Horiguchi, K. Shimizu, T. Kurashima, M. Tateda, and Y. Koyamada, *Development of a distributed sensing technique using Brillouin scattering*, J. Lightwave Technol. **13**, 1296 (1995).
[12] P. Suni and J. Falk, *Theory of phase conjugation by stimulated Brillouin scattering*, J. Opt. Soc. Am. B **3**, 1681 (1986).
[13] P. Hu, J. Goldstone, and S. Ma, *Theoretical study of phase conjugation in stimulated Brillouin scattering*, J. Opt. Soc. Am. B **6**, 1813 (1989).
[14] L. Lombard, A. Brignon, J.-P. Huignard, E. Lallier, and P. Georges, *Beam cleanup in a self-aligned gradient-index Brillouin cavity for high-power multimode fiber amplifiers*, Opt. Lett. **31**, 158 (2006).
[15] C. W. Ballmann, J. V. Thompson, A. J. Traverso, Z. Meng, M. O. Scully, and V. V. Yakovlev, *Stimulated Brillouin scattering microscopic imaging*, Sci. Rep. **5**, 18139 (2015).
[16] N. T. Otterstrom, R. O. Behunin, E. A. Kittlaus, Z. Wang, and P. T. Rakich, *A silicon Brillouin laser*, Science **360**, 1113 (2018).
[17] P. T. Rakich, C. Reinke, R. Camacho, P. Davids, and Z. Wang, *Giant enhancement of stimulated Brillouin scattering in the subwavelength limit*, Phys. Rev. X **2**, 011008 (2012).
[18] B. J. Eggleton, C. G. Poulton, and R. Pant, *Inducing and harnessing stimulated Brillouin scattering in photonic integrated circuits*, Adv. Opt. Photonics **5**, 536 (2013).
[19] H. Shin, W. Qiu, R. Jarecki, J. A. Cox, R. H. Olsson III, A. Starbuck, Z. Wang, and P. T. Rakich, *Tailorable stimulated Brillouin scattering in nanoscale silicon waveguides*, Nat. Commun. **4**, 1944 (2013).
[20] B. J. Eggleton, C. G. Poulton, P. T. Rakich, M. J. Steel, and G. Bahl, *Brillouin integrated photonics*, Nat. Photonics **13**, 664 (2019).
[21] D. J. Richardson, J. Nilsson, and W. A. Clarkson, *High power fiber lasers: Current status and future perspectives*, J. Opt. Soc. Am. B **27**, B63 (2010).
[22] M. N. Zervas and C. A. Codemard, *High power fiber lasers: A review*, IEEE J. Sel. Top. Quantum Electron. **20**, 219 (2014).
[23] S. Fu, W. Shi, Y. Feng, L. Zhang, Z. Yang, S. Xu, X. Zhu, R. Norwood, and N. Peyghambarian, *Review of recent progress on single-frequency fiber lasers*, J. Opt. Soc. Am. B **34**, A49 (2017).

[24] C. Pannell, P. S. J. Russell, and T. Newson, *Stimulated Brillouin scattering in optical fibers: The effects of optical amplification*, J. Opt. Soc. Am. B **10**, 684 (1993).

[25] Y. Panbhiharwala, A. V. Harish, D. Venkitesh, J. Nilsson, and B. Srinivasan, *Investigation of temporal dynamics due to stimulated Brillouin scattering using statistical correlation in a narrow-linewidth cw high power fiber amplifier*, Opt. Express **26**, 33409 (2018).

[26] K. Wisal, S. C. Warren-Smith, C.-W. Chen, R. Behunin, H. Cao, and A. D. Stone, *Generalized theory of SBS in multimode fiber amplifiers*, in *Physics and Simulation of Optoelectronic Devices XXX* (SPIE, Bellingham, WA, 2022), p. PC1199504.

[27] C.-W. Chen, K. Wisal, P. Ahmadi, A. D. Stone, and H. Cao, *Suppressing stimulated Brillouin scattering by selective mode excitation in multimode fibers*, in *CLEO: QELS_Fundamental Science* (Optica Publishing Group, 2022), pp. FF2L–3, https://opg.optica.org/abstract.cfm?uri=CLEO_QELS-2022-FF2L.3.

[28] C.-W. Chen, L. V. Nguyen, K. Wisal, S. Wei, S. C. Warren-Smith, O. Henderson-Sapir, E. P. Schartner, P. Ahmadi, H. Ebendorff-Heidepriem, A. D. Stone, D. J. Ottaway, and H. Cao, *Mitigating stimulated Brillouin scattering in multimode fibers with focused output via wavefront shaping*, Nat. Commun. **14**, 7343 (2023).

[29] W.-W. Ke, X.-J. Wang, and X. Tang, *Stimulated Brillouin scattering model in multi-mode fiber lasers*, IEEE J. Sel. Top. Quantum Electron. **20**, 305 (2014).

[30] C. G. Poulton, R. Pant, and B. J. Eggleton, *Acoustic confinement and stimulated Brillouin scattering in integrated optical waveguides*, J. Opt. Soc. Am. B **30**, 2657 (2013).

[31] L. Dong, *Formulation of a complex mode solver for arbitrary circular acoustic waveguides*, J. Lightwave Technol. **28**, 3162 (2010).

[32] V. Supradeepa, *Stimulated Brillouin scattering thresholds in optical fibers for lasers linewidth broadened with noise*, Opt. Express **21**, 4677 (2013).

[33] J. B. Coles, B.-P. Kuo, N. Alic, S. Moro, C.-S. Bres, J. C. Boggio, P. Andrekson, M. Karlsson, and S. Radic, *Bandwidth-efficient phase modulation techniques for stimulated Brillouin scattering suppression in fiber optic parametric amplifiers*, Opt. Express **18**, 18138 (2010).

[34] Y. Liu, Z. Lv, Y. Dong, and Q. Li, *Research on stimulated Brillouin scattering suppression based on multifrequency phase modulation*, Chin. Optic. Lett. **7**, 29 (2009).

[35] N. Yoshizawa and T. Imai, *Stimulated Brillouin scattering suppression by means of applying strain distribution to fiber with cabling*, J. Lightwave Technol. **11**, 1518 (1993).

[36] A. Liu, *Suppressing stimulated Brillouin scattering in fiber amplifiers using nonuniform fiber and temperature gradient*, Opt. Express **15**, 977 (2007).

[37] A. Kobyakov, S. Kumar, D. Q. Chowdhury, A. B. Ruffin, M. Sauer, S. R. Bickham, and R. Mishra, *Design concept for optical fibers with enhanced SBS threshold*, Opt. Express **13**, 5338 (2005).

[38] P. D. Dragic, C.-H. Liu, G. C. Papen, and A. Galvanauskas, *Optical fiber with an acoustic guiding layer for stimulated Brillouin scattering suppression*, in *Proceedings of the Conference on Lasers and Electro-Optics, 2005* (IEEE, New York, 2005), Vol. 3, pp. 1984–1986.

[39] M.-J. Li, X. Chen, J. Wang, S. Gray, A. Liu, J. A. Demeritt, A. B. Ruffin, A. M. Crowley, D. T. Walton, and L. A. Zenteno, Al/Ge *co-doped large mode area fiber with high SBS threshold*, Opt. Express **15**, 8290 (2007).

[40] T. Hawkins, P. Dragic, N. Yu, A. Flores, M. Engholm, and J. Ballato, *Kilowatt power scaling of an intrinsically low Brillouin and thermo-optic Yb-doped silica fiber*, J. Opt. Soc. Am. B **38**, F38 (2021).

[41] K. Shiraki, M. Ohashi, and M. Tateda, *Suppression of stimulated Brillouin scattering in a fibre by changing the core radius*, Electron. Lett. **31**, 668 (1995).

[42] C. Robin and I. Dajani, *Acoustically segmented photonic crystal fiber for single-frequency high-power laser applications*, Opt. Lett. **36**, 2641 (2011).

[43] S. J. Augst, J. K. Ranka, T. Fan, and A. Sanchez, *Beam combining of ytterbium fiber amplifiers*, J. Opt. Soc. Am. B **24**, 1707 (2007).

[44] T. H. Loftus, A. M. Thomas, P. R. Hoffman, M. Norsen, R. Royse, A. Liu, and E. C. Honea, *Spectrally beam-combined fiber lasers for high-average-power applications*, IEEE J. Sel. Top. Quantum Electron. **13**, 487 (2007).

[45] A. Buikema, F. Jose, S. J. Augst, P. Fritschel, and N. Mavalvala, *Narrow-linewidth fiber amplifier for gravitational-wave detectors*, Opt. Lett. **44**, 3833 (2019).

[46] B. Ward, C. Robin, and I. Dajani, *Origin of thermal modal instabilities in large mode area fiber amplifiers*, Opt. Express **20**, 11407 (2012).

[47] O. Tzang, A. M. Caravaca-Aguirre, K. Wagner, and R. Piestun, *Adaptive wavefront shaping for controlling nonlinear multimode interactions in optical fibres*, Nat. Photonics **12**, 368 (2018).

[48] E. Deliancourt, M. Fabert, A. Tonello, K. Krupa, A. Desfarges-Berthelemot, V. Kermene, G. Millot, A. Barthélémy, S. Wabnitz, and V. Couderc, *Wavefront shaping for optimized many-mode Kerr beam self-cleaning in graded-index multimode fiber*, Opt. Express **27**, 17311 (2019).

[49] M. Shutova, A. D. Shutov, A. A. Zhdanova, J. V. Thompson, and A. V. Sokolov, *Coherent Raman generation controlled by wavefront shaping*, Sci. Rep. **9**, 1565 (2019).

[50] U. Teğin, B. Rahmani, E. Kakkava, N. Borhani, C. Moser, and D. Psaltis, *Controlling spatiotemporal nonlinearities in multimode fibers with deep neural networks*, APL Photonics **5**, 030804 (2020).

[51] C.-W. Chen, K. Wisal, Y. Eliezer, A. D. Stone, and H. Cao, *Suppressing transverse mode instability through multimode excitation in a fiber amplifier*, Proc. Natl. Acad. Sci. U.S.A. **120**, e2217735120 (2023).

[52] M. Plöschner, T. Tyc, and T. Čižmár, *Seeing through chaos in multimode fibres*, Nat. Photonics **9**, 529 (2015).

[53] W. Xiong, P. Ambichl, Y. Bromberg, B. Redding, S. Rotter, and H. Cao, *Spatiotemporal control of light transmission through a multimode fiber with strong mode coupling*, Phys. Rev. Lett. **117**, 053901 (2016).

[54] R. Florentin, V. Kermene, J. Benoist, A. Desfarges-Berthelemot, D. Pagnoux, A. Barthélémy, and J.-P. Huignard, *Shaping the light amplified in a multimode fiber*, Light Sci. Appl. **6**, e16208 (2017).

[55] A. D. Gomes, S. Turtaev, Y. Du, and T. Čižmár, *Near perfect focusing through multimode fibres*, Opt. Express **30**, 10645 (2022).

[56] K. Tei, Y. Tsuruoka, T. Uchiyama, and T. Fujioka, *Critical power of stimulated Brillouin scattering in multimode optical fibers*, Jpn. J. Appl. Phys. **40**, 3191 (2001).

[57] V. I. Kovalev and R. G. Harrison, *Waveguide-induced inhomogeneous spectral broadening of stimulated Brillouin scattering in optical fiber*, Opt. Lett. **27**, 2022 (2002).

[58] M. Sjöberg, M. L. Quiroga-Teixeiro, S. Galt, and S. Hård, *Dependence of stimulated Brillouin scattering in multimode fibers on beam quality, pulse duration, and coherence length*, J. Opt. Soc. Am. B **20**, 434 (2003).

[59] A. Minardo, R. Bernini, and L. Zeni, *Experimental and numerical study on stimulated Brillouin scattering in a graded-index multimode fiber*, Opt. Express **22**, 17480 (2014).

[60] N. Wang, J. Alvarado-Zacarias, M. S. Habib, H. Wen, J. Antonio-Lopez, P. Sillard, A. Amezcua-Correa, A. Schülzgen, R. Amezcua-Correa, and G. Li, *Mode-selective few-mode Brillouin fiber lasers based on intramodal and intermodal SBS*, Opt. Lett. **45**, 2323 (2020).

[61] K. Y. Song and Y. H. Kim, *Characterization of stimulated Brillouin scattering in a few-mode fiber*, Opt. Lett. **38**, 4841 (2013).

[62] B. Srinivasan, G. P. Agrawal, D. Venkitesh *et al.*, *Role of the modal composition of pump in the multi-peak Brillouin gain spectrum in a few-mode fiber*, Opt. Commun. **494**, 127052 (2021).

[63] H. Lü, P. Zhou, X. Wang, and Z. Jiang, *Theoretical and numerical study of the threshold of stimulated Brillouin scattering in multimode fibers*, J. Lightwave Technol. **33**, 4464 (2015).

[64] C.-W. Chen, K. Wisal, M. Fink, A. D. Stone, and H. Cao, *Exploiting spacetime symmetry in dissipative nonlinear multimode amplifiers for output control*, arXiv:2402.10345.

[65] D. Cotter, *Stimulated Brillouin scattering in monomode optical fiber*, J. Opt. Commun. **4**, 10 (1983).

[66] P. D. Dragic and B. G. Ward, *Accurate modeling of the intrinsic Brillouin linewidth via finite-element analysis*, IEEE Photonics Technol. Lett. **22**, 1698 (2010).

[67] W. Qiu, P. T. Rakich, H. Shin, H. Dong, M. Soljačić, and Z. Wang, *Stimulated Brillouin scattering in nanoscale silicon step-index waveguides: A general framework of selection rules and calculating SBS gain*, Opt. Express **21**, 31402 (2013).

[68] C. Wolff, M. J. Steel, B. J. Eggleton, and C. G. Poulton, *Stimulated Brillouin scattering in integrated photonic waveguides: Forces, scattering mechanisms, and coupled-mode analysis*, Phys. Rev. A **92**, 013836 (2015).

[69] Y. Shi, A. Cerjan, and S. Fan, *Invited article: Acousto-optic finite-difference frequency-domain algorithm for first-principles simulations of on-chip acousto-optic devices*, APL Photonics **2**, 020801 (2017).

[70] V. Laude and J.-C. Beugnot, *Lagrangian description of Brillouin scattering and electrostriction in nanoscale optical waveguides*, New J. Phys. **17**, 125003 (2015).

[71] J. D. Jackson, *Classical Electrodynamics* (John Wiley & Sons, New York, 2021).

[72] D. Nelson and M. Lax, *Theory of the photoelastic interaction*, Phys. Rev. B **3**, 2778 (1971).

[73] B. A. Auld, *Acoustic Fields and Waves in Solids* (1973).

[74] L. D. Landau, E. M. Lifšic, E. M. Lifshitz, A. M. Kosevich, and L. P. Pitaevskii, *Theory of Elasticity* (Elsevier, New York, 1986), Vol. 7.

[75] A. Feldman, *Relations between electrostriction and the stress-optical effect*, Phys. Rev. B **11**, 5112 (1975).

[76] B. Ndagano, R. Brüning, M. McLaren, M. Duparré, and A. Forbes, *Fiber propagation of vector modes*, Opt. Express **23**, 17330 (2015).

[77] K. Okamoto, *Fundamentals of Optical Waveguides* (Elsevier, New York, 2021).

[78] A. W. Snyder and W. R. Young, *Modes of optical waveguides*, J. Opt. Soc. Am. **68**, 297 (1978).

[79] COMSOL MULTIPHYSICSv. 5.5, http://www.comsol.com, Comsol ab, Stockholm, Sweden.

[80] S. Bittner, S. Guazzotti, Y. Zeng, X. Hu, H. Yılmaz, K. Kim, S. S. Oh, Q. J. Wang, O. Hess, and H. Cao, *Suppressing spatiotemporal lasing instabilities with wave-chaotic microcavities*, Science **361**, 1225 (2018).

[81] R. Waldron, *Some problems in the theory of guided microsonic waves*, IEEE Trans. Microwave Theory Tech. **17**, 893 (1969).

[82] P.-L. Giscard, K. Lui, S. Thwaite, and D. Jaksch, *An exact formulation of the time-ordered exponential using path-sums*, J. Math. Phys. (N.Y.) **56**, 053503 (2015).

[83] M. Mermelstein, S. Ramachandran, J. Fini, and S. Ghalmi, *SBS gain efficiency measurements and modeling in a* 1714 μm *2 effective area LP_{08} higher-order mode optical fiber*, Opt. Express **15**, 15952 (2007).

[84] M. O. Van Deventer and A. J. Boot, *Polarization properties of stimulated Brillouin scattering in single-mode fibers*, J. Lightwave Technol. **12**, 585 (1994).

[85] C. Jauregui, C. Stihler, S. Kholaif, Y. Tu, and J. Limpert, *Mitigation of transverse mode instability in polarization maintaining, high-power fiber amplifiers*, in *Fiber Lasers XVIII: Technology and Systems* (SPIE, Bellingham, WA, 2021), Vol. 11665, pp. 147–152.

[86] K. Wisal, C.-W. Chen, Z. Kuang, O. D. Miller, H. Cao, and A. D. Stone, *Optimal input excitations for suppressing nonlinear instabilities in multimode fibers*, arXiv:2407.05201.

[87] K.-P. Ho, *Exact model for mode-dependent gains and losses in multimode fiber*, J. Lightwave Technol. **30**, 3603 (2012).

[88] W. Xiong, P. Ambichl, Y. Bromberg, B. Redding, S. Rotter, and H. Cao, *Principal modes in multimode fibers: Exploring the crossover from weak to strong mode coupling*, Opt. Express **25**, 2709 (2017).

[89] R. Paschotta, J. Nilsson, A. C. Tropper, and D. C. Hanna, *Ytterbium-doped fiber amplifiers*, IEEE J. Quantum Electron. **33**, 1049 (1997).

[90] K. Wisal, C.-W. Chen, H. Cao, and A. D. Stone, *Theory of transverse mode instability in fiber amplifiers with multimode excitations*, APL Photonics **9**, 066114 (2024).

[91] E. Garmire, *Perspectives on stimulated Brillouin scattering*, New J. Phys. **19**, 011003 (2017).

[92] H. Cao, T. Čižmár, S. Turtaev, T. Tyc, and S. Rotter, *Controlling light propagation in multimode fibers for imaging, spectroscopy, and beyond*, Adv. Opt. Photonics **15**, 524 (2023).

[93] K.-P. Ho and J. M. Kahn, *Linear propagation effects in mode-division multiplexing systems*, J. Lightwave Technol. **32**, 614 (2013).

[94] S. H. Chang, H. S. Chung, N. K. Fontaine, R. Ryf, K. J. Park, K. Kim, J. C. Lee, J. H. Lee, B. Y. Kim, and Y. K. Kim, *Mode division multiplexed optical transmission enabled by all–fiber mode multiplexer*, Opt. Express **22**, 14229 (2014).

[95] V. L. Iezzi, S. Loranger, A. Harhira, R. Kashyap, M. Saad, A. Gomes, and S. Rehman, *Stimulated Brillouin scattering in multi-mode fiber for sensing applications*, in *Proceedings of the Workshop on Fibre and Optical Passive Components* (IEEE, New York, 2011), pp. 1–4.

[96] Z. Liu, L. G. Wright, D. N. Christodoulides, and F. W. Wise, *Kerr self-cleaning of femtosecond-pulsed beams in graded-index multimode fiber*, Opt. Lett. **41**, 3675 (2016).

[97] K. Krupa, A. Tonello, B. M. Shalaby, M. Fabert, A. Barthélémy, G. Millot, S. Wabnitz, and V. Couderc, *Spatial beam self-cleaning in multimode fibres*, Nat. Photonics **11**, 237 (2017).

[98] D. K. Biegelsen, *Photoelastic tensor of silicon and the volume dependence of the average gap*, Phys. Rev. Lett. **32**, 1196 (1974).

[99] W. Voight, *Lehrbuch der Kristallphysik* (Teubner, Leipzig, 1928).

[100] O. Slezák, A. Lucianetti, and T. Mocek, *Tensor-to-matrix mapping in elasto-optics*, J. Opt. Soc. Am. B **37**, 1090 (2020).

[101] W. S. Slaughter, *The Linearized Theory of Elasticity* (Springer Science & Business, New York, 2012).

[102] A. H. McCurdy, *Modeling of stimulated Brillouin scattering in optical fibers with arbitrary radial index profile*, J. Lightwave Technol. **23**, 3509 (2005).

[103] P. D. Dragic, *Estimating the effect of* Ge *doping on the acoustic damping coefficient via a highly* Ge*-doped MCVD silica fiber*, J. Opt. Soc. Am. B **26**, 1614 (2009).

[104] M. Smith, B. Kuhlmey, C. M. de Sterke, C. Wolff, M. Lapine, and C. Poulton, *Metamaterial control of stimulated Brillouin scattering*, Opt. Lett. **41**, 2338 (2016).

[105] Q. Liu, *Literature Review: Materials with Negative Poisson's Ratios and Potential Applications to Aerospace and Defence* (DSTO Victoria, Australia, 2006).

[106] P. Dainese, P. S. J. Russell, N. Joly, J. Knight, G. Wiederhecker, H. L. Fragnito, V. Laude, and A. Khelif, *Stimulated Brillouin scattering from multi-GHz-guided acoustic phonons in nanostructured photonic crystal fibres*, Nat. Phys. **2**, 388 (2006).